

pubs.acs.org/JPCB Article

# Photon Activation of Glassy Dynamics: A Mechanism for Photoinduced Fluidization, Aging, and Information Storage in Amorphous Materials

Published as part of The Journal of Physical Chemistry virtual special issue "Peter J. Rossky Festschrift". Vassiliy Lubchenko\* and Peter G. Wolynes\*



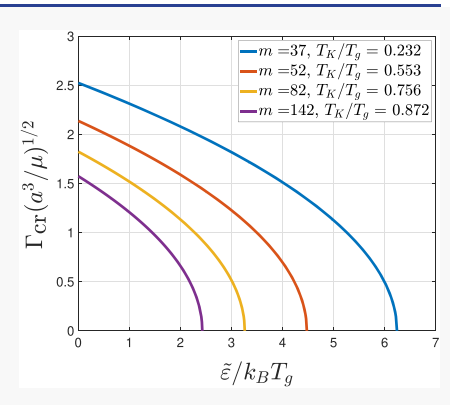
Cite This: J. Phys. Chem. B 2020, 124, 8434-8453



**ACCESS** 

Metrics & More

ABSTRACT: We discuss the photon activation of structural relaxations in glassy melts and frozen glasses containing molecules that can photoisomerize. The built-in stress following a photoinduced electronic transition lowers the thermal activation barrier for subsequent structural reconfiguration of the glassy matrix. We provide explicit predictions for the barrier distribution and structural relaxation spectrum as functions of the concentration of photoactivated molecules and the fragility of the material. The typical barrier decreases upon photoactivation, while the barrier distribution increases in width with increasing mole fraction of photoactive molecules and fluence, and becomes multimodal. In a frozen glass, the initial effects of photoisomerization locally facilitate the dynamics near the excited chromophores and can lead to complete fluidization at a sufficiently high fluence. Photon activation initially decreases the yield strength of the glass. Depending on the precise time course of illumination, there however emerges a spatial coexistence of softened regions with regions that, after being destabilized by



Article Recommendations

illumination, have reconfigured so that they are now made of ultrastable glass or have crystallized as in a porcelain. This sequence of events, after illumination, can lead to highly stable amorphous solids, potentially approaching the Kauzmann limit. These mechanisms are at the root of optical information storage technologies in amorphous materials.

#### I. INTRODUCTION

The slow molecular motions of glasses and supercooled liquids take place through activated events. It is awkward to try to explain the steep temperature dependence of molecular mobility without invoking some kind of energy barrier crossing. The near-Arrhenius nature of the temperature dependence of those molecular motions that still occur just below the laboratory glass transition temperature—a fact often ignored by many theorists—makes the case for the importance of activated processes in glasses truly unequivocal. From where does the activation energy needed to overcome the barriers in the energy landscape come? Ordinarily, the activation energy is borrowed from the thermal vibrational motions of the molecules. Physical chemists have long known that activation energy may not only come from heat but can alternatively come from the absorption of light.<sup>1,2</sup> Indeed, over the last century, much has been learned about how molecular-activated events occur by initiating chemical reactions through the absorption of photons.<sup>3,4</sup> The absorption of a photon deposits some of the excitation energy into vibrations, but some energy also becomes deposited in conformational changes or bond breaking. Photoactivation can then initiate further reaction events and configurational changes. 1,2 While the immediate consequences of absorbing a photon are intrinsically quantum mechanical in nature, the subsequent events can often be understood classically. In this paper, we explore the consequences of photochemical initiation events on the classical reconfiguration processes in glasses and supercooled liquids, using the random first-order transition (RFOT) theory, 5,6 which highlights activated processes, as a guide.

While our concerns in this paper are largely theoretical, we would be remiss not to point out that understanding the sequelae of photon absorption in glasses is of importance to many technological problems ranging from photonics<sup>7</sup> and optical data storage in holograms<sup>8</sup> to energy storage<sup>9</sup> to the degradation of glassy plastics in the environment.<sup>10</sup> In sufficiently intense light, chalcogenide glasses have been shown to age<sup>11,12</sup> and even flow<sup>7,13,14</sup> at temperatures much below their thermal glass transition. These systems also can

Received: July 16, 2020 Revised: August 27, 2020 Published: August 28, 2020





photocrystallize. 15 Illumination of amorphous silicon carbide surfaces has been shown to cause reconfiguration events, which have been followed with scanning microscopy. <sup>16</sup> Understanding the photoinitiation processes for these systems is complicated by the richness of the electronic structures of amorphous semiconductors both in the ground and the excited states. 17-21 A somewhat simpler example of photon-activated dynamics is provided by organic glasses that contain azobenzene dyes. Upon the absorption of light, these intensely colored dye molecules undergo conformational changes analogous to the cis to trans photochemical isomerization in stilbene, the study of which has illuminated many aspects of energy flow in molecules as well as frictional effects on reaction dynamics in condensed phases.<sup>22–27</sup> While the electronic structure issues for these organic systems are more manageable than the issues for the amorphous inorganic semiconductors, quantum-chemical studies still continue to reveal intriguing intricacies. 28,29 Owing to these complexities, we will focus on the events immediately following photon activation in glasses, in the present paper, though some qualitative conclusions will also be made for the case of extended illumination.

The present analysis suggests that, for the purpose of analyzing the subsequent classical motions, the photinitiation process can be thought of as storing strain energy in the local vicinity of the light-absorbing molecule. This strain energy then becomes available to allow further local reconfiguration events on the amorphous energy landscape, which can then be described using the random first-order transition theory of glasses. 5,6 The RFOT theory envisions the primary activated events in glasses and supercooled liquids as the nucleation of alternative aperiodic packings in an initial aperiodic structure selected from the energy landscape.<sup>30</sup> The RFOT theory shows there are two main classes of activated events that merge together near the crossover temperature, often referred to as  $\alpha$ and  $\beta$ -relaxations. The  $\alpha$ -relaxations involve the motions of relatively compact clusters containing  $\sim\!200$  molecules near the laboratory glass transition temperature  $T_g$ . The  $\beta$ -relaxation, coming from the low-energy tail of the barrier height distribution, arises through the rearrangement of percolation clusters or strings that involve motions of a smaller number of particles, typically. <sup>31,32</sup> These two styles of rearrangement merge near a spinodal-like crossover to collisional motion.

The localized character of all these activated motions implies that, at sufficiently low concentrations of the chromophores, the effects of photon absorption are also quite heterogeneous; only the reconfiguration events that occur near to the photoisomerized molecules can be activated by light. This additional heterogeneity, in turn, implies there will be a distinct dependence of the nature and distribution of the photoactivated motions of glasses not only on the concentration of absorbers but also on the total amount of light absorbed as well as the time course of its absorption. Since photoactivation shifts the distribution of the rates of reconfiguration events only in the direct vicinity of the absorbers, one finds typically a markedly bivariate distribution of relaxation times. In addition, after a photoactivated region has reconfigured, the local environment of the chromophore will relax to a new state on the energy landscape, one more characteristic of those found at the ambient temperature, which is typically lower than the original fictive temperature of the glass. The distribution of relaxation times then becomes multivariate, because subsequent motions now will have higher barriers. The mosaic picture of RFOT theory predicts, then, that photoactivated glasses will display

significantly more dynamical heterogeneity than even thermally activated glasses do already, having some regions being much less stable than the average, 33 while other regions will have become rather more stable. Heterogeneous relaxation has been pointed out in computational studies of model systems, 34–36 but computational investigations have been confined to higher temperatures than those characteristic of glasses in the laboratory.

The complex interplay of both softening and hardening of different regions in glasses then depends on the detailed history of illumination and relaxation. In this paper we will not treat this interplay in detail but, rather, will focus primarily on the immediate sequelae of photoactivation for two specific situations that describe only what happens immediately following an intense, but brief, pulse of light. In the first, we will discuss the case where the illumination is so intense and the density of photoactive molecules is so high that several photonically induced excitations have taken place in a single dynamically correlated region. Separately, we will discuss the case where only a few photons have been absorbed, which leads to well-separated photon-activated regions in the glass. In this regime, photactivated molecules can be thought of as sites of heterogeneous nucleation for structural reconfigurations. We will also comment on the further consequences of photoactivated barrier crossing, which leads to a very heterogeneous mixture of regions in the glass, some of which are "ultrastable."37-39 These effects imply that continuous illumination and aging will change the mechanical behavior of glasses either to harden them or to soften them depending on the illumination protocols. This protocol complexity explains many puzzling results in the technological literature concerning photochemical information storage. The description can be straightforwardly generalized also to include external shear, which we show will further speed up photoinduced fluidization and aging.

#### II. MICROSCOPIC MODEL

For concreteness, we will consider a solution containing photoactive molecules that can switch between two distinct stereoisomeric states. Notable examples of such molecules include a variety of diimide-, diphosphene-, or ethylenecontaining molecules that can switch between the cis and trans isomers of the double-bonded subunits. Much as for other photochemical processes,<sup>28</sup> photoinduced isomerization in a glassy material can be thought of as resulting from motion through a conical intersection on an upper energy surface. It is useful to consider two limiting cases with regard to the effects of the environment of the photoisomerizing molecule. For a rapidly relaxing solvent, the isomerization involves internal rotations of the molecule. These rotations are well-approximated by motion along solvent-averaged energy surfaces that are rather close to the Born-Oppenheimer surfaces in the gas phase with, perhaps, solvation corrections due to the polarization of the solvent, see Figure 1. In the minimal description, then, there is at least one internal angular variable, call it  $\phi_{\mathrm{m}}$ , reflecting the relative orientation of the two units connected by the rotatable bond. To simplify the following discussion, we keep in mind an azobenzene or resveratrol-like molecule as the photoactive species, but many of the conclusions are general and would apply, for instance, to the more complex photophysics of the chalcogenides. In the case of the azobenzene isomerization, a convenient choice for the reaction coordinate  $\varphi_{\rm m}$  is the dihedral angle formed by the planes containing the two aromatic units. The two stereoisomers of azobenzene correspond to the minima

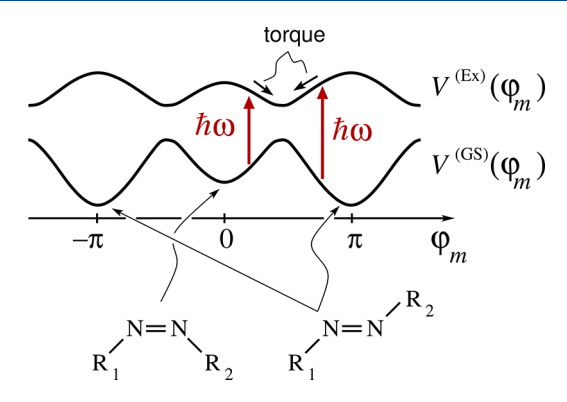


Figure 1. A schematic showing how torque is generated following the photoexcitation of a photoisomerizable molecule in a fast solvent. At the bottom of the figure, we show the stereoisomers corresponding to specific minima on the electronic ground-state energy surface.  $R_1$  and  $R_2$  denote some molecular units such as benzene rings. The angular coordinate  $\varphi_m$  corresponds with the rotation angle for the double bond connecting the two nitrogen atoms.

on the electronic ground-state surface  $V^{(GS)}(\varphi_m)$  in Figure 1. Immediately following photoexcitation, the molecule finds itself on an excited-state potential surface  $V^{(\mathrm{Ex})}(arphi_{\mathrm{m}})$ , in accordance with the Franck-Condon principle. The minima on the excitedstate surface generally do not coincide exactly with those on the ground-state surface, as we illustrate schematically in Figure 1. Because vibrational motions are fast, the molecule will often be able to reach the minimum on the excited potential surface before it electronically de-excites to the ground case, as in Neukirch et al.<sup>29</sup> The excited-state minimum is close to the col separating the ground-state minima. Thus, following the eventual electronic de-excitation through the conical intersection, the molecule will fall on either side of the col with comparable probability. As a result, the quantum efficiency of isomerization can be as large as 50%, as is the case in the study in ref 40. Last but not least, we note that, according to ref 29, the highest occupied molecular orbital (HOMO) and lowest unoccupied molecular orbital (LUMO) energies vary by as much as 2 eV, respectively, during isomerization. These figures provide, then, an upper-bound estimate for the energy differential between the relevant extrema on the potential energy surfaces in Figure 1.

The opposite extreme limit is that of a very "stiff" solvent, which cannot relax significantly during these intramolecular motions. Now, rather than simply exerting friction, the effectively frozen solvent gives rise to a distribution of perturbed energy surfaces for isomerization. For some solvent configurations, isomerization can not proceed until the environment also moves so as to conform to the target isomer state. For other configurations, the molecule can still rearrange. To describe the distribution energy surfaces requires additional variables reflecting the locally broken symmetries of the environment: The energy now depends not only on the relative orientation of the aromatic groups bridged by the isomerizable bond but also on how each ring moves with respect to the environment in which the ring was originally trapped. In a simplest description for the broken symmetry environment, we can define rotation angles for each ring,  $\varphi_1$  and  $\varphi_2$ , and the respective potential energies of interaction with the environment as  $V_1(\varphi_1)$  and  $V_2(\varphi_2)$ . The molecular isomerization coordinate is simply the difference between  $\varphi_2$  and  $\varphi_1$ .

$$\varphi_{\rm m} = \varphi_2 - \varphi_1 \tag{1}$$

The gas-phase energies are functions of this difference variable alone, but in the frozen environment, the energy function becomes less symmetric

$$\begin{split} V^{(i_{\rm e})}(\varphi_{\rm l},\,\varphi_{\rm 2}) &= V^{(i_{\rm e})}(\varphi_{\rm 2}-\varphi_{\rm l}) \,+\, V_{\rm l}^{(i_{\rm s})}(\varphi_{\rm l}-\varphi_{\rm l}^{(i_{\rm s})}) \\ &+\, V_{\rm 2}^{(i_{\rm s})}(\varphi_{\rm 2}-\varphi_{\rm 2}^{(i_{\rm s})}) \end{split} \tag{2}$$

where  $V^{(j_e)}(\varphi)$  is the electronic potential energy from Figure 1, which would govern the isomerization of the standalone molecule in the absence of the restoring elastic force from the matrix but, of course, including solvent polarizability. The superscript " $(j_e)$ " labels the electronic state. The energy terms  $V_1$  and  $V_2$ , which account for the restoring force from the matrix, depend on the identity of the current aperiodic free energy minimum, hence the label " $(i_s)$ ". The depths, locations, and the curvatures of these minima vary from one aperiodic minimum to another and are distributed random variables, to be discussed shortly.

All three functions on the right-hand side (rhs) of eq 2 are periodic with period  $2\pi$ . By construction,  $V^{(j_e)}(\varphi_m)$  has at least two minima, within a single period, which are generally nondegenerate. The functions  $V_1$  and  $V_2$  could conceivably have one or more minima, depending on the shape of the corresponding molecular unit. For the sake of concreteness, we will assume that both functions  $V_1(\varphi)$  and  $V_2(\varphi)$  have just one minimum located at  $\varphi=0$ . We illustrate the energy function (2) for the ground electronic surface in Figure 2 and for an excited

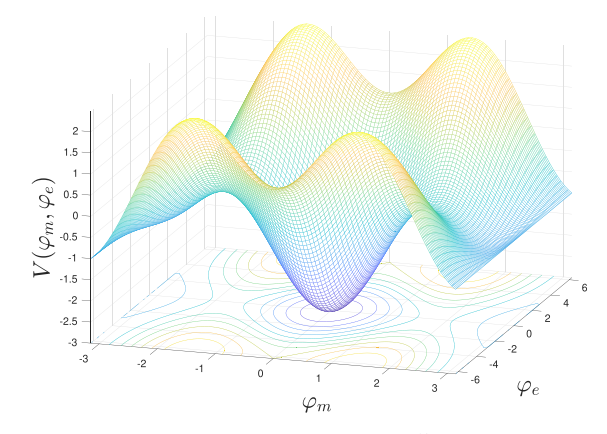


**Figure 2.** Potential surface from eq 2, with  $V^{(i)}(\varphi) = -\cos(2\varphi)$  and  $V_1(\varphi) = V_2(\varphi) = -\cos(\varphi)$ . This specific  $V^{(i)}(\varphi)$  is intended to illustrate the ground-state electronic term.

state in Figure 3. It seems instructive to use not the variables  $\varphi_1$  and  $\varphi_2$  as the arguments but, instead, their linear combinations: the torsion angle  $\varphi_{\rm m}$  from eq 1 and the orthogonal coordinate  $\varphi_{\rm e}$   $\equiv \varphi_1 + \varphi_2$ . We set  $\varphi_1^{(i_*)} = \varphi_2^{(i_*)} = 0$  in Figures 2 and 3, for concreteness.

In Figure 4, we schematically depict the energy of the molecule-plus-environment along the slice  $\varphi_{\rm e}=0$ , for the ground and an excited electronic energy surface. We observe that, when added to the intrinsic potential for rotating the bond, the solvent-induced confining potential will destabilize the minimum of the excited-state surface while moving its location sideways, toward the minimum of the ground-state surface. For a sufficiently stiff matrix, the excited-state minimum may disappear altogether. At the same time, the matrix-induced potential will raise the energy of the ground-state transition state and will displace its auxiliary minimum. These displacements of

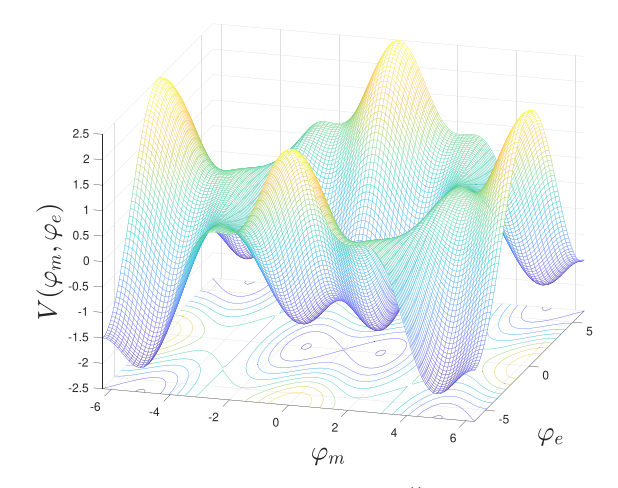


**Figure 3.** Potential surface from eq 2, with  $V^{(i)}(\varphi) = 0.5 \cdot \cos(2\varphi)$  and  $V_1(\varphi) = V_2(\varphi) = -\cos(\varphi)$ . This specific  $V^{(i)}(\varphi)$  is intended to illustrate an excited-state electronic term.

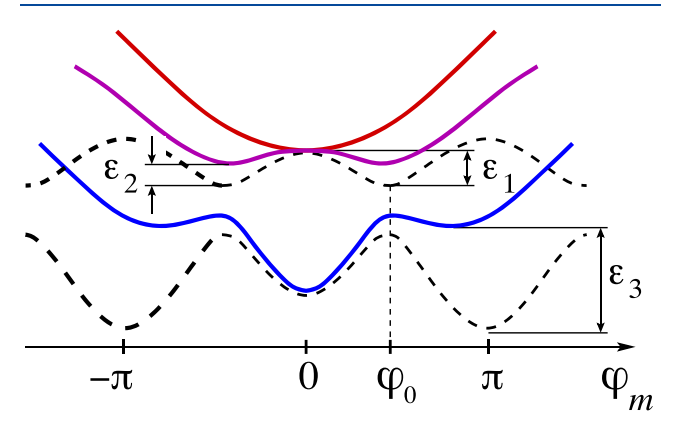


**Figure 4.** A schematic showing how built-in strain can be generated when an isomerizable molecule is embedded in a stiff solvent. The dashed lines are the energy surfaces from the Figure 1, which include the high-frequency response of the solvent. The solid lines include the contribution of the restoring force from the environment and correspond with the  $\varphi_e \equiv \varphi_1 + \varphi_2 = 0$  slice of the energy surfaces from Figures 2 and 3. We do not show a configuration in which the matrix is so stiff that the alternative minimum on the lower energy surface is removed.

the minima result in a decrease of the quantum yield for isomerization, relative to the mobile solvent case, consistent with observation. 40 The aforementioned destabilization of the minima on the potential surfaces implies there will now be a built-in stress. The magnitude  $\varepsilon_{\rm i}$  of this photoinduced stress energy is shown graphically in Figure 4 for three distinct realizations of the effective molecule-plus-environment potential acting on the variable  $\phi_{\mathrm{m}}.$  In one realization, the restoring force of the matrix is so high that the electronically excited configuration does not even have a metastable minimum. The resulting built-in stress energy is graphically indicated with the quantity  $\varepsilon_1$ . If the matrix is not too stiff, so that the upper surface retains a metastable minimum, the resulting built-in stress will be lower. The magnitude of this stress energy is shown with the quantity  $\varepsilon_2$  on Figure 4. This realization corresponds to the energy surface shown in Figure 3. The quantity  $\varepsilon_3$  gives the builtin stress energy corresponding to a situation when the molecule returns to the electronic ground state before the matrix relaxes, as in Figure 2. The quantity  $\varepsilon_3$  is clearly the largest of the three  $\varepsilon_1$ parameters; however, the probability of landing in the

corresponding configuration is the lowest, too. Note also that, if the matrix-induced additional potential is sufficiently steep, then there is no metastable minimum on the ground-state surface in the first place (this unlikely situation is not shown).

The built-in stress on the excited surface can be relaxed either by falling into a lower-energy electronic state and/or reconfiguring the environment. The vibrational relaxation of the environment is generally fast, following Kasha's rule. 41 The remaining stress energy can then power further structural rearrangements, the main subject of this paper. For instance, to structurally relax the metastable configuration corresponding to the quantity  $\varepsilon_2$  in Figure 4, the torsional variable  $\varphi_m$  must achieve a magnitude of nearly  $\pi/2$ . For this to happen, the environment must rearrange so that the quantity  $(\varphi_1^{(i_s)} - \varphi_2^{(i_s)})$ also changes by  $\pi/2$ . To relax to the configuration corresponding to the quantity  $\varepsilon_3$  in Figure 4 may thus require more than one reconfiguration event between different aperiodic minima of the molecule-solvent system. Typically in a reconfiguration event, solvent molecules move only a Lindemann length, 42 which is approximately one-tenth of the interparticle spacing.

One can bound the magnitude of the built-in stress energy by noting that the energy of the vertical electronic transition is numerically close to 2 eV ( $\lambda \lesssim 500$  nm). Thus, Figure 4 suggests that the photoinduced built-in stress energy per chromophore  $\varepsilon_{\rm ph}$  will be, numerically, only a fraction, but perhaps not too small a fraction, of an electronvolt and in any event can be sizably larger than  $k_{\rm B}T$ . To be explicit, one may write down an approximation for the energy function (2) near the (shifted) bottom of an electronically excited energy surface to determine  $\varepsilon_2$  in Figure 4.

$$V(\varphi_{\rm m}) = V_0 + \frac{k_{\rm e}}{2} (\varphi_2 - \varphi_1 - \varphi_0)^2$$
(3)

$$+\frac{k_{\rm s}}{2}(\varphi_1-\varphi_1^{(i_{\rm s})})^2+\frac{k_{\rm s}}{2}(\varphi_2-\varphi_2^{(i_{\rm s})}) \tag{4}$$

In this harmomic approximation, the  $V^{(j_e)}$  term has been expanded around the minimum, located at  $\varphi_0$  in the absence of the elastic component of the solvent response; see Figure 4. The spring constant  $k_{\rm e}$  is the curvature of the electronic energy at this minimum. Likewise, we retain only the quadratic term in the response of the matrix, while setting both of the corresponding spring constants to the same value  $k_{\rm s}$ , for simplicity. The quantity  $k_{\rm s}$  depends on the shear modulus  $\mu$  of the material and geometric factors:  $^{43}k_{\rm s}\simeq \mu a^3$ , where a is the appropriate molecular length scale. Minimizing eq 3 with respect to  $\varphi_1$  and  $\varphi_2$  and subtracting  $V_0$ , we obtain the built-in stress energy.

$$\varepsilon_2 = \frac{k_e k_s}{2(2k_e + k_s)} (\varphi_2^{(i_s)} - \varphi_1^{(i_s)} - \varphi_0)^2$$
(5)

As already mentioned, this built-in stress energy will be released when the environment reconfigures so that the relative orientation of the elastic minima for the two benzene rings matches the new position  $\varphi_0$  of the minimum of the electronic surface. For the minimum at  $\varphi_0$  to exist in the first place, one must have  $k_s < k_e$ . Thus,  $k_e k_s / (2k_e + k_s) \simeq k_s / 2$ . Since  $k_s \simeq \mu a^3$  is of the order electronvolt, <sup>44</sup> we see that  $\varepsilon_2$  is less than but perhaps still of the order electronvolt. Note also that the quadratic approximation for the elastic response of the matrix in eq 4 is an overestimate; the actual response scales similarly with the shear modulus but is not as steep in terms of the displacement. Equation 5 can be also used to estimate the magnitude of the

site-specific fluctuations in the magnitude of the photoinduced stress energy. While the quantities  $\varphi_0$  and  $k_{\rm e}$  are fully determined by the quantum electronic structure of the photoactive molecule and can be regarded as fixed, the elastic coefficient  $k_{\rm s}$  and the configurational variables  $\varphi^{(i_{\rm s})}$ , showing how the rings are trapped in the matrix, fluctuate from chromophore to chromophore and from substate to substate of the glassy energy landscape. These fluctuations are, likely, correlated: The specific combination of these two parameters in eq 5 corresponds to the local energy density. We expect that fluctuations of the frozen strain energy are similar in magnitude for distinct electronic surfaces, and, thus, their size is comparable to the equilibrium fluctuations that depend on the molar heat capacity.

In the following, we will write the average built-in stress energy per photoactivated event as

$$\varepsilon_{\rm ph} = C\varepsilon_{\rm i} \le \varepsilon_{\rm i}$$
(6)

In this expression we introduced a numerical constant  $C \le 1$  to account for the possibility that the built-in stress may not be released by a single reconfiguration event. This constant can be treated as a fitting constant in the absence of a detailed structural model of the photoactivated molecule in its environment.

# III. STRUCTURAL DYNAMICS AND THE EFFECTS OF PHOTOACTIVATION

The photoinduced built-in stress modifies the subsequent structural relaxation of the molecular environment around the chromophore. As discussed in the Introduction, glassy systems structurally relax via cooperative, activated events that are quantitatively described by the random first-order transition theory. We briefly review some pertinent aspects of the RFOT description of activated glassy dynamics; detailed accounts can be found in refs 5 and 6.

# A. Review of Pertinent Notions of the RFOT Theory.

Activated reconfigurations of molecular glasses can each be thought of as a spatially contiguous sequence of displacements of rigid molecular units. Each such unit may be called a "bead." When a bead moves, the displacement is generically near the limit of the mechanical stability, which is often called the Lindemann length.  $^{42}$  The number N of beads that have already moved is a convenient progress coordinate that measures the changes in glassy structure. Since the initial state of a reconfiguration is a specific energy minimum chosen out of many, individual bead moves are typically energetically uphill in the beginning of the reconfiguration process but are entropically stabilized, because there are many ways to choose where to place the particles as they move. The free energy becomes downhill past a certain size  $N^{\ddagger}$ .  $N^{\ddagger}$  thus corresponds to the bottleneck. A series of energy increments resulting from these individual moves can be approximated as a continuous curve; several examples are sketched in Figure 5. To avoid confusion we note that the "energy" coordinate in Figure 5 is actually the Gibbs free energy for escaping from an individual vibrational minimum; 45,46 see also below. The individual free energy activation profiles vary throughout the glass, because they depend on the initial configuration.

The typical free energy profile can be described as a continuous function of N that depends also on the shape of the reconfiguring region in physical space. Reconfiguring regions can have many shapes, being relatively compact near the Kauzmann temperature  $T_{\rm K}$ , but being more diaphanous at temperatures near the dynamical transition to collisional

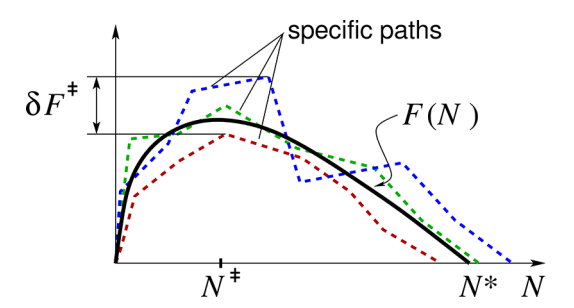


**Figure 5.** A schematic showing a typical free energy profile from eq 7 (smooth line) and three example profiles emanating from a specific location, including the effects of driving force fluctuations.

motion. In a frozen glass, the free energy profile also depends on the energy of the initial state, which, for shallow quenches, can be described using one additional parameter, specifically, the fictive temperature.  $^{30,47-49}$  In the mean-field version of the RFOT theory, the transition to collisional transport is a spinodal and is describable with critical exponents, etc. That spinodal however becomes a soft crossover in actual glasses, which are finite-dimensional systems. This crossover occurs near a temperature  $T_{\rm cr}$ , which can be predicted by the RFOT theory.  $^{31,50,51}$  The high-barrier subset of reconfiguration events that dominate relaxation in equilibrated melts at temperatures below  $T_{\rm cr}$  become generally larger and relatively more compact as the temperature decreases. For the more compact reconfiguration events, the typical free energy profile for reconfiguring a region of size N contains two contributions.  $^{30,44,52}$ 

$$F(N) = \gamma N^{1/2} + \Delta g N \tag{7}$$

The first quantity,  $\gamma N^{1/2} > 0$ , reflects the typical mismatch penalty between the reconfigured region and the surrounding matrix, which is only elastically displaced with distortions less than the Lindemann length. We point out, in passing, that there remains some controversy on the mismatch energy exponent, but this is not important for the discussion here. The term  $\Delta gN$  is negative in sign; it is the Gibbs free energy difference between the set of target configurations and the initial configuration and thus reflects the bulk driving force for escape from the local metastable configuration.

The most probable activation barrier following from the nucleation profile, eq 7, then becomes

$$F_{\alpha,\rm mp}^{\ddagger} = \frac{\gamma^2}{-4\Delta g} \tag{8}$$

The subscript  $\alpha$  indicates that the high-barrier, compact reconfigurations correspond with what is usually called the primary, or  $\alpha$ -relaxation, process. The critical nucleation size of the reconfiguring region is

$$N^{\ddagger} = \left(\frac{\gamma}{2\Delta g}\right)^2 \tag{9}$$

The overall size of the final reconfiguration event, that is, the cooperativity size  $N^*$ , is determined by the condition that the free energy vanishes:  $F(N^*) = 0$ . In other words, at size  $N^*$  a thermodynamically available target state with the same energy as the original configuration will be found with probability one; thus there is no specific tendency to grow the region further. (Tunneling between such states provides a mechanism for the

infamous two-level systems seen in amorphous solids. 44,55) One then finds

$$N^* \equiv (\xi/a)^3 = \left(\frac{\gamma}{\Delta g}\right)^2 = 4N^{\ddagger} \tag{10}$$

where we also defined the volumetric size  $\xi$  of the cooperatively reconfiguring region.

Above the kinetic glass transition, new configurations are always becoming available, so the initial configuration is chosen out of a fully equilibrated distribution. In the equilibrated liquid, therefore, the driving force toward a new local configuration is entirely entropic in origin<sup>52,56</sup>

$$\Delta g_{\rm eq} = -Ts_{\rm c} \tag{11}$$

where  $s_c$  is the configurational entropy per particle; the quantity  $e^{Ns_c/k_B}$  gives the number of distinct free energy minima available to a region of size N. While there remain disputes regarding how to best define  $s_c$  in finite dimensions, the configurational entropy is tolerably well approximated by the difference between the entropy of a glassy melt and the corresponding crystal, since the bulk of the vibrational frequencies of the crystal and the glass are not very different. In a nonequilibrium glass, the initial configuration is metastable with respect to the equilibrium ensemble at the same temperature, and therefore the driving force generally has an additional enthalpic component.  $^{30,45}$ 

$$\Delta g = \Delta h - \Delta (Ts) \tag{12}$$

For glasses quenched from the melt,  $\Delta h$  depends on the so-called fictive temperature of the glass and the configurational heat capacity  $\Delta c_{\rm p} = T(\partial s_{\rm c}/\partial T)$ :  $\Delta h \approx \Delta c_{\rm p}(T-T_{\rm f})$ ; see also below.

Local fluctuations of the activation profile result from local variations in both the initial energy and the fluctuations of the configurational entropy of structures that are available for reconfiguration. These fluctuations lead to a broadening of the barrier distribution. The broadening toward the high-barrier side is cut off, because the environment around any especially slow regions actually will have already rearranged on a typical time scale and thus have changed the boundary conditions on the reconfiguration event.<sup>33</sup> Bhattacharya, Bagchi, and Wolynes have shown how this effect, which might be called "facilitation," can be described using an extended mode-coupling theory that accounts for activated events. 57,58 Rather than using this formalism, here we employ approximate expressions for the lpharelaxation barrier distribution due to Lubchenko.<sup>59</sup> For the present purposes, the Lubchenko approximation is more convenient than the earlier approximation for the facilitation cutoff introduced by Xia and Wolynes.<sup>33</sup> Thus

$$p^{(\alpha)}(F^{\ddagger}) = \begin{cases} \frac{c_1}{\tilde{F}^2} e^{-(1/\tilde{F}-1)^2/2\delta\tilde{F}^2}, & \tilde{F} \leq \tilde{F}_e \\ \frac{c_2}{\tilde{F}^2} e^{\tilde{F}/(\delta\tilde{F}/4)}, & \tilde{F}_e < \tilde{F} \leq 1 \\ 0, & \tilde{F} > 1 \end{cases}$$
(13)

where  $\tilde{F} \equiv F^{\ddagger}/F_{\alpha,\mathrm{mp}}^{\ddagger} < 1^{+}$  is the barrier scaled by its most probable value, and the constants  $\tilde{F}_{\mathrm{e}}$ ,  $c_{1}$ , and  $c_{2}$  are determined by requiring that the distribution be normalized and be continuous, as well as have its first derivative continuous at the first break point, too. The relative size of the fluctuations in the barrier

$$\delta \tilde{F} \equiv \frac{\delta F^{\ddagger}}{F_{\alpha,\text{mp}}^{\ddagger}} = \frac{\delta g}{|\Delta g|} \tag{14}$$

directly follows from the fluctuations of the driving force (per particle)  $\delta g$ .

$$\delta g = \delta(\Delta g) \equiv \delta f(N^*)^{-1/2} \tag{15}$$

eq 15 reflects the fact that the fluctuation  $\delta g$  of the intensive quantity  $\Delta g$  scales as  $N^{-1/2}$  with the region size N. The size-independent quantity  $\delta f$  in eq 15 is then identified with the square root of the variance of the driving force per particle. By eq 10, the *relative* barrier fluctuation does not explicitly depend on the cooperativity size.

$$\delta \tilde{F} \equiv \frac{\delta F^{\ddagger}}{F_{\alpha,\text{mp}}^{\ddagger}} = \frac{\delta f}{\gamma} \tag{16}$$

In the thermally equilibrated regime, the quantity  $\delta f$  is determined by fluctuations in the configurational entropy at the cooperativity size. <sup>30,33</sup>

$$\delta f = T[k_{\rm B}\Delta c_{\rm p}(T)]^{1/2} \tag{17}$$

The quantity  $\Delta c_{\rm p}(T)$  is the (temperature-dependent) configurational heat capacity of the liquid. It is numerically close to the excess liquid heat capacity of the liquid relative to the corresponding crystal. Below the glass transition, the fluctuations in the driving force can be approximated using the same expression using the frozen-in value of  $\Delta c_{\rm p}(T)$  at  $T_{\rm g}$  while setting  $T=T_{\rm g}$  in eq 17. We note that both the Lubchenko and Xia-Wolynes approximations introduce sharp cutoffs that are smoothed out in the more accurate treatment of facilitation effects by the extended mode-coupling theory.  $^{57,58}$ 

There is always an entropic advantage for allowing the reconfiguring region to vary in shape. As the system approaches the dynamical transition temperature the reconfiguring region becomes less compact owing to the entropic advantage of diaphanous shapes. (The most compact shape, a sphere, is unique and thus has no shape entropy.) These shape fluctuations resemble percolation clusters or stringlike objects. For either percolation clusters or for stringlike reconfigurations, because of their large interfacial areas, the free energy penalty for creating them scales linearly with the number N of particles that have been displaced.  $^{31,45}$ 

$$F(N) = \gamma' N + \Delta g N - k_{\rm B} T(\ln \Omega) N \equiv \phi N \tag{18}$$

The mismatch coefficient  $\gamma'$  for the diaphanous clusters is proportional to that for compact clusters:  $\gamma' = c_{\gamma}\gamma$ . This magnitude of the mismatch coefficient reflects the enthalpic cost of breaking a requisite number of bonds for moving a particle. This mismatch energetic penalty, though, is ameliorated by the entropic advantage of forming such noncompact shapes at higher temperature. The quantity  $\Omega$  reflects the multiplicity of strings that can emanate from a given locale. Given the modest size of N in liquids in the laboratory, the two limiting cases from eqs 7 and (18) are expected to cover the full range of region shapes well.

While the free energy profile for compact reconfiguration events is nonmonotonic, at a given temperature, the profile for the diaphanous clusters, eq 18, is monotonic, either increasing or decreasing with N depending on the sign of  $\phi$ . The special value  $\phi = 0$  signals the crossover from activated transport to largely collisional transport.<sup>31</sup>

String growth becomes downhill above the crossover temperature  $T_{\rm cr}$ , where  $\phi < 0$ , after paying a one-particle initiation cost  $F_{\rm in}$ . Like the free energy in eq 18, this initiation cost accounts both for the enthalpy of bond breaking and the driving force but does not contain the entropic contribution  $\ln \Omega$  from differing shapes, because exactly one particle must be moved to initiate the reconfiguration.

$$F_{\rm in} = \gamma' + \Delta g \tag{19}$$

When  $\phi$  > 0, that is, at temperatures below the crossover, the stringy excitations can only grow to a finite extent. Despite being positive on average, the energy cost of one step in a stringlike motion is, however, distributed, so atypical low-barrier processes can always take place. These weakly activated processes give rise to the so-called  $\beta$ -relaxations. They are also responsible for the deviations from the VTF (Vogel-Tammann-Fulcher) law near the crossover, which can be detected by the Stickel plot. The corresponding barrier distribution was worked out by Stevenson and Wolynes. It is given by

$$p^{(\beta)}(F^{\ddagger}) = q \frac{\sinh(F_{\text{in}}q)}{\sinh^{2}(F^{\ddagger}q)}, \quad (F_{\text{in}} < F^{\ddagger} < F_{\alpha,\text{mp}}^{\ddagger})$$
(20)

where

$$q = \frac{1}{\delta f} \left( \frac{2}{N_{\text{s,max}}} + \frac{\phi^2}{\delta f^2} \right)^{1/2} = \frac{1}{\delta f} \left( \frac{2\phi}{F_{\alpha,\text{mp}}^{\ddagger}} + \frac{\phi^2}{\delta f^2} \right)^{1/2}$$
(21)

where  $\delta f$  is from eq 15. More about this distribution can be found in Appendix C.  $N_{\rm s,max}$  is the maximum string length, which is determined by the merging with the compact  $\alpha$ -event distribution. <sup>32,61</sup>

$$N_{\rm s,max} = F_{\alpha,\rm mp}^{\ddagger}/\phi \tag{22}$$

We indicated, in eq 20, that the barrier is distributed between its smallest value, the initiation cost  $F_{\rm in}$ , and the most probable value  $F_{\alpha,\rm mp}^{\ddagger}$  of the  $\alpha$ -relaxation barrier, because larger barriers will, again, be wiped out by facilitation effects.

The distribution for  $\beta$ -relaxation processes that come from the stringlike motions is not normalized to one, because the distribution is cut off by overlap with the compact  $\alpha$ -relaxation events. The weight of the distribution of  $\beta$ -events is given by (see Appendix C)

$$\Psi = \frac{\sinh[(F_{\alpha,\text{mp}}^{\ddagger} - F_{\text{in}})q]}{\sinh(F_{\alpha,\text{mp}}^{\ddagger}q)} \le 1$$
(23)

This weight increases with temperature reaching a value that depends on the initiation cost  $1-F_{\rm in}/F_{\alpha,\rm mp}^{\ddagger}<1$  as the crossover is approached from below, which formally corresponds with the limit  $\phi$ ,  $q\to 0$ . At the crossover temperature, the distribution of barriers (20) tends to a power law,  $p^{(\beta)}(F^{\ddagger}) \simeq F_{\rm in}/(F^{\ddagger})^2$  implying a very broad distribution of relaxation times,  $\propto (\tau \ln^2(\tau/\tau_0))^{-1}$ , nearly a 1/f spectrum. In the usual expression for the waiting time of an activated process

$$\tau = \tau_0 e^{F^{\ddagger}/k_{\rm B}T} \tag{24}$$

the prefactor  $\tau_0$  is a vibrational time scale and is on the order of a picosecond. <sup>62</sup>

Though historically derived using separate arguments, the  $\alpha$ and  $\beta$ -relaxation processes are not strictly distinct; rather, they
represent the limiting varieties of a complete family of

reconfiguration events. For practical purposes, we will take them as contributing to the overall relaxation spectrum in a roughly additive fashion

$$p(F^{\ddagger}) = \frac{1}{1 + \Psi} [p^{(\alpha)}(F^{\ddagger}) + p^{(\beta)}(F^{\ddagger})]$$
(25)

where the factor in front of the square brackets will take care, after the fact, of the overall normalization; the quantity  $\Psi$  is from eq 23. For the thermally activated cases, both the  $\alpha$ -and  $\beta$ -components of the overall barrier distribution are cut off at  $F_{\rm in}$  on the low-barrier side. The initiation cost  $F_{\rm in}$  remains positive below the crossover,  $\phi>0$ , according to eqs 18 and (19), and reaches its lowest value of  $k_{\rm B}T\ln\Omega$  at the crossover itself. Finally we note that, in the glassy state, the driving force for reconfiguration can be increased by applying an external stress. Under stress, the condition  $\phi=0$  with the additional driving force determines the yield strength.  $^{45,63,64}$ 

**B.** The Spatially Averaged Photoactivation Regime. When the concentration of photoactive molecules is high, after also a high fluence of light is absorbed, each reconfigurable region will have taken on similar amounts of photoinduced stress. The average of this stored energy can be roughly determined by spatially averaging over the photoexcited molecules. We see that photoactivation in this regime leads to a substantial additional *bulk* driving force for reconfiguration that depends on the concentration of photoisomerized molecules

$$\Delta g_{\rm ph} = \Delta g - \tilde{\varepsilon} \tag{26}$$

In this expression  $\Delta g$  < 0 is the driving force, per bead, from eq 7 while the quantity

$$\tilde{\varepsilon} \equiv (n_{\rm ph}a^3)\varepsilon_{\rm ph} \tag{27}$$

The average built-in stress energy due to photoactivation, per bead, depends on the residual stress left by photoisomerization and the concentration  $n_{\rm ph}$  of photoisomerized units.  $\varepsilon_{\rm ph}$  is the built-in stress energy left by a photoactivation event that can be released in a single reconfiguration event, as discussed in Section II

The additional driving force  $-\tilde{e}$  plays a role analogous to that of the excess energy in a nonequilibrium glass that has been frozen-in at a higher glass transition temperature than the ambient temperature<sup>30</sup> or that has been introduced by placing the glass under external mechanical stress. The magnitude of the spatially averaged built-in mechanical stress energy  $\tilde{e}$  is determined by the probability  $p_{\rm ph} = n_{\rm ph} a^3$  to find a photoactive unit at a given location. We estimate that, for pure azobenzene, this probability would maximally be  $\sim$ 0.3, assuming that each of the benzene rings and the azo unit can be taken to comprise an effectively spherical bead. For azobenzene solutions, then, we have  $p_{\rm ph} \lesssim 0.3$ . We note that, in principle,  $\tilde{e}$  can be measured calorimetrically by determining the heat release when a photoactivated glass is heated.

With the averaged stored energy for bulk photoactivation, the most probable barrier for compact  $\alpha$ -relaxation processes is then modified according to

$$F_{\alpha,\text{mp,ph}}^{\ddagger} = \frac{\gamma^2}{-4\Delta g_{\text{ph}}} \tag{28}$$

Likewise the driving force for reconfiguration events that have the shapes of percolation clusters is increased.

$$\phi_{\rm ph} = \gamma' + \Delta g_{\rm ph} - k_{\rm B} T(\ln \Omega) \tag{29}$$

We see that photoinduced isomerization speeds up both the  $\alpha$ -and  $\beta$ -relaxations. On the one hand, the typical  $\alpha$ -relaxation barrier remains finite but can be greatly reduced. The  $\beta$ -relaxation processes, on the other hand, may eventually become downhill through photoactivation, for sufficiently high fluence, eventually causing full photofluidization. Note that the initiation cost  $F_{in}$  is also decreased by photoactivation

$$F_{\rm in,ph} = \gamma' + \Delta g_{\rm ph} \tag{30}$$

but remains positive below the crossover,  $\phi > 0$ , according to eq 29.

When considering the dynamics, however, we must account not only for the averages but also for the fact that photoactivated units are not distributed uniformly in space. This gives rise to additional fluctuations around the typical reconfigurational free energy profile in eq 26. To the lowest-order approximation, the excess strain energy follows a binomial distribution for the number of isomerized units, implying the variance of the additional stress energy is proportional to  $p_{\rm ph}(1-p_{\rm ph})$ . The driving force  $\varepsilon_{\rm ph}$  will also vary from chromophore to chromophore, because the restoring forces from the environment are distributed with a standard variation  $\delta\varepsilon_{\rm ph}$ . After we add these contributions, the variance of the driving force, per particle, increases after irradiation, cf. eq 15.

$$\delta f_{\rm ph}^2 = k_{\rm B} T^2 \Delta c_p + n_{\rm ph} a^3 (1 - n_{\rm ph} a^3) \varepsilon_{\rm ph}^2 + n_{\rm ph} a^3 \delta \varepsilon_{\rm ph}^2$$
(31)

To calculate the resulting relaxation spectrum in the spatially averaged regime, then, one can still employ the general formula from eqs 25–(31), by simply modifying the parameters of the  $\alpha$ -and  $\beta$ -processes to account for the effects of photoactivation.

In order for the spatially averaging argument in the Section to be strictly valid, the quantity  $n_{\rm ph}a^3$  cannot be too small; otherwise, the sample can no longer be regarded as even approximately homogeneous. We will turn to this dilute regime shortly. At high fluence, however, the photoactivation-caused corrections in eqs 26 and (31) can be very significant. Indeed,  $\Delta g$  is of order  $k_B T$ . The built-in stress energies  $\varepsilon_{\rm ph}$  are of order  $10^1 k_B T$ , and  $n_{\rm ph} a^3$  can be as large as 0.3; therefore, the photoinduced destabilization can be significantly greater than the inherent driving forces for thermal reconfiguration. We therefore see that photoactivation can destroy barriers entirely, thus leading to photofluidization.

The effects of the additional broadening of the barrier distribution reflected in eq 31 are significant, too. Indeed, the quantity  $\Delta c_p$  ranges from  $0.25k_B$  for very strong liquids to more than  $10k_B$  for very fragile liquids (per bead). 52 As discussed in Section II, the magnitude of the fluctuations  $\delta arepsilon_{
m ph}$  in the built-in photoinduced stress energy is also expected to be close in magnitude to that of the thermal energy fluctuations, whose variance scales as  $\Delta c_v^{43}$  and thus the photoinduced fluctuations are numerically as significant as the first term on the rhs of eq 31. The direct fluctuations from photoactivation however are scaled down by the factor  $n_{\rm ph}a^3$ . Thus, we expect the fluctuations due to varying the number of photoactivated units make the most significant contribution to the broadening of the barrier distribution. In view of the large magnitude of this term, proportional to  $\tilde{\varepsilon}$ , the presence of even a single isolated excited moiety in a reconfiguring region will significantly change the

barrier distribution, making even a very strong material behave like a very fragile liquid.

To illustrate the above ideas in an experimentally relevant context we adopt a specific parametrization for the materials properties that will be used over the full temperature range below the crossover:  $0 < T < T_{\rm cr}$ ; see Appendix A for details. The energies are shown in units of the laboratory glass transition temperature  $T_{\rm g}$ . The deviations of the T-dependence of the  $\alpha$ -relaxation time from the strictly Arrhenius form, that is, how fragile or strong the liquid is, will be quantified using the conventional fragility index  $m = \partial \log_{10} \tau / \partial (T_{\rm g}/T)$ . The elastic properties of the glass enter through the Poisson ratio  $\sigma$ . The latter ratio will be set at 0.25 throughout. For the temperature dependence of the configurational entropy, again for concreteness, we will use the Richert-Angell fit  $^{65,66}$ 

$$s_{\rm c} \simeq \Delta c_{\rm p} T_{\rm g} (1/T_{\rm K} - 1/T) \tag{32}$$

where  $T_{\rm K}$  is the so-called Kauzmann temperature, and  $\Delta c_{\rm p}$  is the heat capacity jump at  $T_{\rm g}$ . Thus, the T-dependence of configurational heat capacity is simply  $\Delta c_{\rm p}(T) = \Delta c_{\rm p}(T_{\rm g}/T)$ . Note that the RFOT theory correctly predicts that m and  $\Delta c_{\rm p}$  are related. <sup>52,67</sup>

To determine the value of the driving force  $\Delta g$  in frozen glasses,  $T < T_g$ , we will adopt the usual approximation in which the state of the glass is initially described by using just one additional parameter, which is often called the fictive temperature  $T_{\rm f}$ . The fictive temperature is usually close to the glass transition temperature  $T_{\rm g}$  on the laboratory time scale, where the material fell out of equilibrium on cooling but can be modestly lowered following an extensive amount of annealing and/or aging; here we will set  $T_{\rm f}$  precisely to the laboratory glass transition temperature  $T_{\rm g}$ . For most molecular glass formers, the effects of volume mismatch, on cooling, and vibrational entropy changes during reconfiguration are not very significant. The Gibbs energy stabilization  $\Delta g$  from eq 12 comes largely from the configurational degrees of freedom. Using eqs 12 and (32), one obtains for the driving force

$$\frac{\Delta g(T)}{\Delta c_{p} T_{g}} = \begin{cases}
\ln(T/T_{g}), & (T < T_{K}) \\
\ln(T/T_{g}) + (1 - T/T_{K}), & (T_{K} \leq T < T_{g}) \\
(1 - T/T_{K}), & (T_{g} < T)
\end{cases}$$
(33)

where we used that the additional enthalpic drive is  $\Delta h = \int \Delta c_{\rm p}$  dT. By construction, the Kauzmann state is the glassy state with the lowest enthalpy. In actuality, additional processes may occur in the amorphous solid, such as nanocrystallization<sup>68</sup> or other types of local ordering. We will not quantify these in the present paper.

First we determine the dependence of the RFOT crossover temperature  $T_{\rm cr}$  on the amount of built-in stress energy. This dependence can be experimentally tested using the observation that, below the crossover, many transport phenomena begin to become decoupled. S1,59,69 When the effective  $T_{\rm cr}(\tilde{\epsilon})$  becomes less than  $T_g$ , the glass also will flow easily, that is, fluidize. Setting  $\phi|_{T=T_{\rm cr}}=0$  in eq 29 straightforwardly yields the dependence of  $T_{\rm cr}$  on the stored energy density due to photoactivation. In Figure 6, we show the dependence of the effective crossover temperature on photoinduced stored stress energy for select values of the fragility index that cover the experimentally observed range. According to the discussion in Section B, the

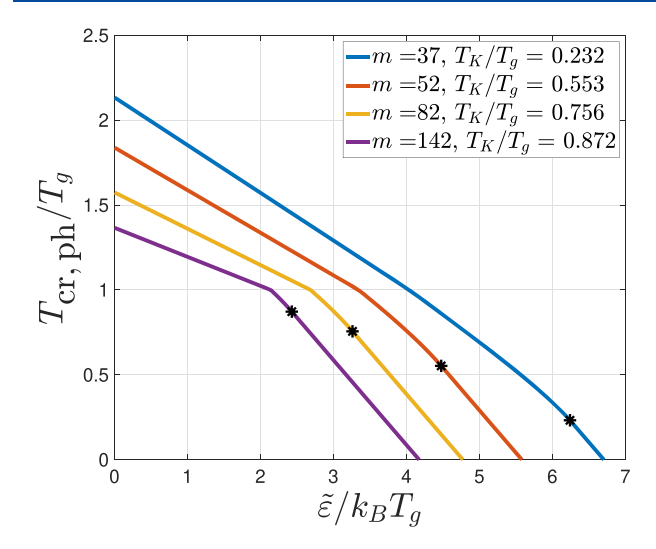


**Figure 6.** Dependence of the temperature of the crossover from the activated to the collisional transport is plotted against the magnitude of the built-in photoactivated stress energy for select values of the fragility index. The corresponding values of  $T_{\rm K}$  are indicated in the legend and are shown on the graph with the asterisks.

magnitude of  $\tilde{\epsilon}$  is unlikely to exceed  $3k_{\rm B}T_{\rm g}$  or so. Nonetheless we observe that very fragile substances can easily be fluidized even at temperatures substantially below the thermal glass transition at  $T_{\rm g}$ . In contrast, we expect that stronger substances will still exhibit activated transport, after photoactivation, which nonetheless will still be quite a lot faster that one would expect from pure thermal activation. As we shall see also, the strength of the glass will be compromised by photoactivation, initially.

We first show in Figure 7 three barrier distributions for a fragile liquid at the laboratory glass transition. One distribution

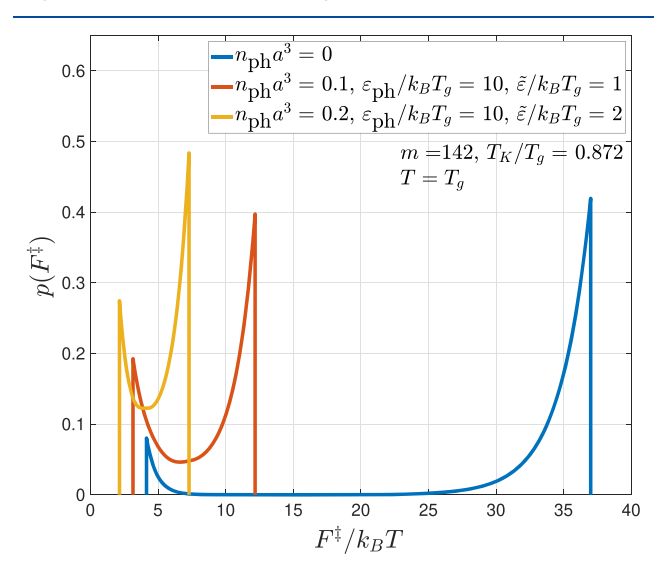


**Figure 7.** Barrier distributions for a very fragile substance at  $T = T_{\rm g}$ . The  $n_{\rm ph} = 0$  curve corresponds to a pristine equilibrated fluid, while the  $n_{\rm ph} > 0$  curves correspond to the effective relaxation spectrum in the same liquid but following a short, intense pulse of light.

is for the pristine material, while the other two are for the photoactivated material for two distinct values of the concentration of photoactivated molecules,  $n_{\rm ph} = 0.1$  and  $n_{\rm ph} = 0.2$ , respectively. For both of these illustrative cases, the built-in stress energy per photoactivated event was set at a rather

substantial value  $\varepsilon_{\rm ph}=10k_{\rm B}T$ . According to Figure 6, the  $n_{\rm ph}=0.2$  case corresponds to a situation that is quite near the crossover to collisional transport. We observe that the already substantial  $\beta$ -relaxation tail of the distribution in the pristine material becomes even more pronounced in the photoactivated material. Indeed, the  $\beta$ -and  $\alpha$ -parts of the barrier distribution become comparable in weight near the thermal crossover. The effects of photoactivation on a *strong* substance are shown in Figure 8. While the overall motions do not speed up as much as

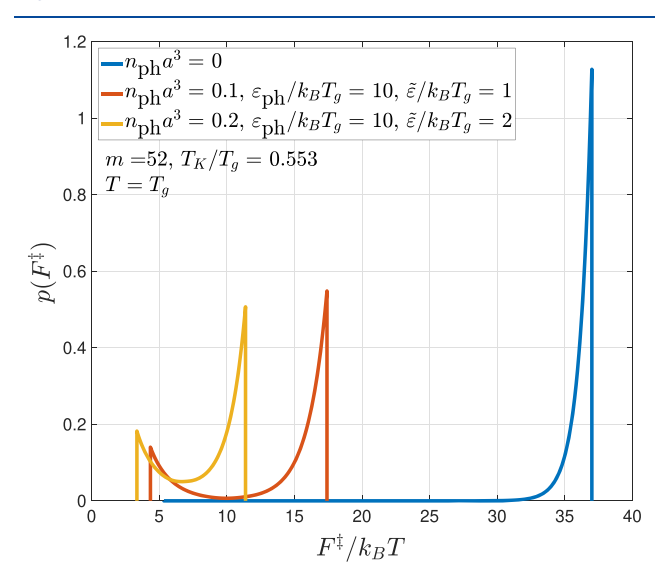


Figure 8. Same as Figure 7, but for a very strong substance.

for the more fragile material, the changes in the shape of the barrier distribution are actually more dramatic for the strong material. While the  $\beta$ -wing of the distribution is virtually absent for a pure strong liquid, after photoactivation the  $\beta$ -wing becomes just as significant, relative to the  $\alpha$ -relaxation, as it is for the thermally activated fragile liquid near the crossover. The theory suggests, then, that photoisomerization will lead to the emergence of  $\beta$ -relaxations in strong substances, which would otherwise be hard to detect. Light makes strong substances behave qualitatively as if they were in fact fragile liquids.

To summarize, whether or not photoactivation can completely eliminate the reconfiguration barriers, motions in the glass or supercooled melt are made much faster by photoactivation. They also become more nonexponential over a substantial temperature range.

We emphasize that the photoactivated relaxation spectra shown in Figures 7 and 8 correspond to a rather specific experimental protocol. These spectra are best thought of as prescribing the structural dynamics immediately after a relatively intense yet fairly short pulse of light. The pulse should be intense enough to create a given amount of built-in stress energy, while the duration of the pulse should be short enough so that little structural relaxation has been able to take place during the pulse itself. The shortest relaxation times for the photoinduced spectra in Figures 7 and 8 are of order 10 psec; so, for a strict comparison, the pulse duration should be on the order of a picosecond or less, a regime quite easily achievable in practice these days

The speed up of the dynamics following a pulse of light is only transient. Under steady illumination, not only both thermal and photoactivated relaxations occur but also regions that have relaxed may absorb additional photons. The resulting dynamics

can be described by a spatially dependent stochastic model that accounts for the kinetics of excitation and de-excitation, both electronic and structural, and the interactions between relaxations that are in close spatial proximity. A quantitative description can be obtained using dynamical equations for fluctuating mobility, <sup>64,70,71</sup> but these must be generalized now for the case where there are two types of regions, namely, "dark" and photoactivated, respectively. The structural effects on the local quantum yield must also be included. In frozen glasses, there is the additional difficulty reflected in the local variations of the fictive temperature. In this paper, we limit ourselves to a brief qualitative discussion of the expected results.

For photoactivation in frozen glasses, eqs 26-(29) and Figure 6 allow us to evaluate the barrier distribution corresponding to the earliest times following an intense pulse of light. In Figure 9,

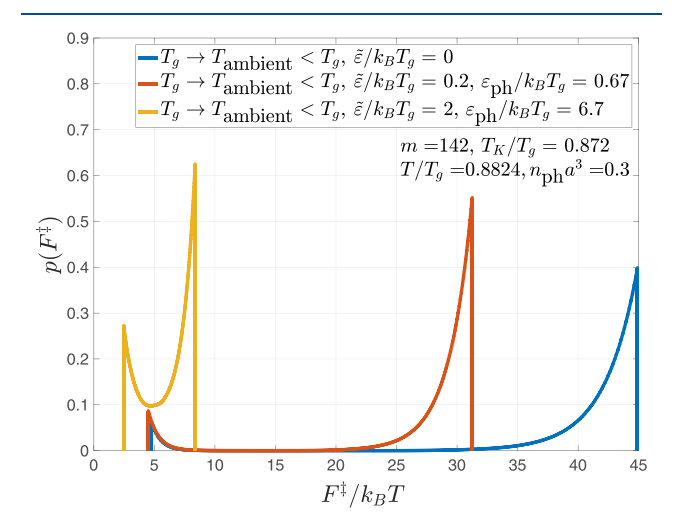


**Figure 9.** Barrier distributions for initial aging events in a fragile glass made by a quench to temperature  $T = T_K + 0.01 \cdot T_g$ , also in the presence of illumination for two values of built-in stress energy.

we show relaxation spectra for the aging of a glass sample that has been rapidly cooled to an ambient temperature below  $T_o$ . One spectrum is for a pristine sample, while the other two spectra are for the same aging process but also in the presence of built-in photoactivated stress produced by a short intense pulse of light, for two distinct values of  $\varepsilon_{\rm ph}$ . We chose the ambient temperature so that it would take a year or so for the pristine sample to show extensive aging. (The aging will be only partial, because the regions neighboring those regions that have already relaxed will be substantially stabilized thus effectively halting further relaxation.) The presence of an extensive low-barrier portion in the photoactivated spectrum implies rapid but local aging. These faster regions will relax toward more stable structures representative of equilibrium at the ambient temperature. This aging process will result in a heterogenious sample made of spatially coexisting regions with varying degrees of

We see that photoinduced built-in stress dramatically speeds up aging. In Figure 10, we show the magnitude of the *steady-state* photoinduced energy stress density such that initial aging events at a specific target temperature  $T_{\rm target} < T_{\rm g}$  occur on the time scale corresponding to the usual laboratory glass transition. On the one hand, for  $T_{\rm target} > T_{\rm K}$ , the target state is representative of the ambient temperature as already pointed out. On the other hand, for  $T_{\rm target} < T_{\rm K}$ , the target state will be an ideal glass with

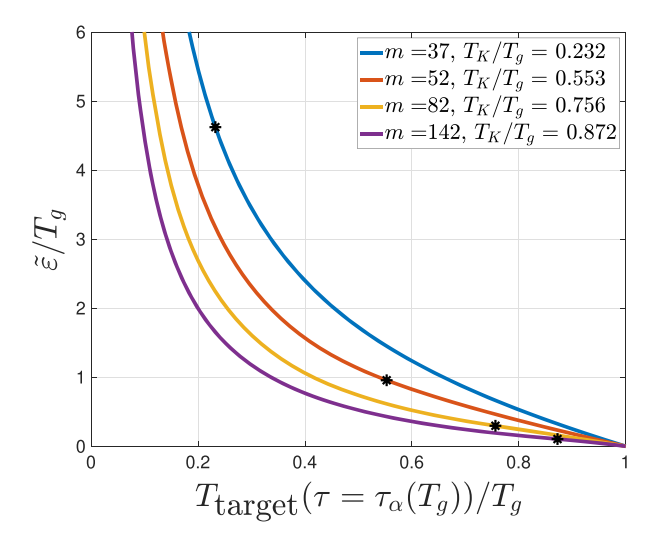


**Figure 10.** Magnitude of photoinduced built-in stress energy needed to drive a glass to a target temperature on the time scale of the laboratory glass transition, for select values of the fragility index. The corresponding values of  $T_{\rm K}$  are indicated in the legend and on the graph, with the asterisks.

properties characteristic of  $T_{\rm K}$ . By eq 8, the necessary photoinduced stress energy  $\tilde{\epsilon}$  is

$$\tilde{\varepsilon} = \Delta g(T) - \frac{\gamma^2(T)}{\gamma^2(T_g)} \frac{T_g}{T} \Delta g(T_g)$$
(34)

Assuming the mismatch coefficient  $\gamma$  is temperature-independent, this yields the results shown in Figure 10. We observe that, even for reasonably modest values of  $\tilde{\epsilon} \approx k_{\rm B}T_{\rm g}$ , rather deep states become kinetically accessible, especially for more fragile substances.

As illumination proceeds at  $T < T_g$ , the glass is first transiently fluidized, as exemplified by the photoactivated spectrum from Figure 9, and subsequently ages to a more stable state. The equilibrium state at  $T < T_g$  would be much more stable than that at  $T_g$ . The typical relaxation barrier in an equilibrated material increases rapidly with lowering the temperature and, in fact, diverges upon approaching the Kauzmann temperature, according to eqs 8, (11), and (32), owing to the lack of alternative structural states.  $^{5,6,56}$  Because of this, such a stable material cannot be obtained practically by cooling a bulk liquid. After photoactivation, the driving force toward equilibrium,  $\Delta g = -Ts_c - \tilde{\varepsilon}$ , does not vanish even at  $T_K$  and below, where  $s_c = 0$ . Indeed, since  $s_c(T_g) \simeq 0.8k_B$ ,  $^{46,52,72}$  we expect for  $\tilde{\varepsilon}$  of order  $k_BT_g$ , even near  $T_K$  the typical barrier for reconfiguration,  $F^{\ddagger} \leq \gamma^2/4\tilde{\varepsilon}$  is not too different from that for an equilibrated melt near  $T_g$ .

Figure 9 also implies that fragile glasses, for which  $T_{\rm K}$  is already close to  $T_{\rm g}$  in the first place, can be partially driven to the lowest-enthalpy glassy state through photoactivation. Once the irradiation has been discontinued, however, the driving force to re-equilibrate would now vanish,  $\Delta g_{\rm ph} \to \Delta g \simeq 0$ . Irradiation eventually then will lead to a dramatic increase in the typical relaxation barrier and, essentially, a complete arrest of the structure. In fact, to melt such an ultrastable structure on a realistic time scale, one will need to heat it well above the original glass transition temperature, because in addition to the usual entropic contribution  $-Ts_{\rm c} < 0$  to the driving force there is now a positive enthalpic contribution:  $\Delta h = \int_{T_{\rm K}}^T \! \Delta c_{\rm p} \; dT$ . The driving force for a transition from a structure equilibrated at temperature

 $T < T_{\rm g}$  to one equilibrated at  $T_{\rm g}$  becomes  $\Delta g = \Delta c_{\rm p} T_{\rm g} [\ln(T_{\rm g}/T) + (1-T_{\rm g}/T_{\rm K})]$ , cf. eq 33. Owing to this increased stability, ultrastable glasses 37-39 tend to rejuvenate by front propagation. 64,70,71

To illustrate the above notions on light-induced softening and the subsequent hardening of frozen glasses, we show in Figure 11

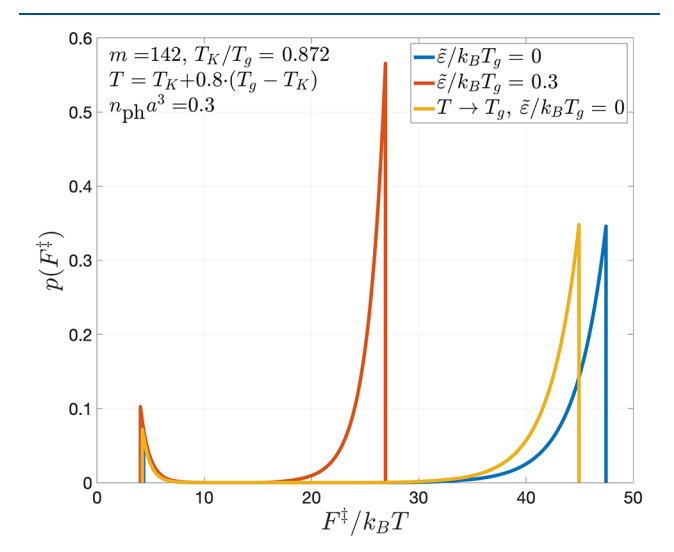


**Figure 11.** Barrier distributions for dynamics at a temperature intermediate between  $T_{\rm g}$  and  $T_{\rm K}$ , without and with built-in photoactivated stress energy. Also the barrier distribution for rejuvenation by heating from that low temperature to  $T_{\rm g}$ , without illumination, is shown.

three relaxation spectra for a very fragile substance at a temperature T below  $T_{\alpha}$  (but above  $T_{\kappa}$ ): (a) for the equilibrated liquid, (b) the same liquid now subject to a built-in photoinduced stress, and (c) the liquid first equilibrated at the same low temperature T and then quickly heated to the glass transition temperature  $T_e$ . We selected the temperature T to be not too low but rather close to  $T_g$  for graphical clarity, so that the photoactivated and dark relaxation spectra can be displayed clearly on the same graph. We observe that the barriers for both equilibrium dynamics at this low temperature and for the dynamics upon rejuvenation to the laboratory glass transition temperature are very high. Bear in mind that  $F^{\ddagger}/k_{\rm B}T = 45$ corresponds to a relaxation time longer than a year. This remarkable stability of the photoaged glass even slightly below  $T_{\sigma}$  can be used, then, to record information using polarized light. Polarized light creates driving forces for the isomerizable units to orient in a particular direction that maximizes the absorption and subsequent structural stabilization. Given this, the photoactivated aging spectra shown in Figure 9 explain the kinetics of the early stages of information writing, which employs linearly polarized light. The spectrum of photoactivated rejuvenation in Figure 11 prescribes the much slower kinetics of photoinduced erasure of optical information, which uses circularly polarized light. Such optical recording and erasure of information using thin films are described in ref 8. The present results also automatically imply that ultrastable glasses should be more photostable, consistent with observation.<sup>73</sup>

Under continuous illumination, photoinduced aging and rejuvenation are rather complicated, because the glass becomes a time-dependent superposition of *four* types of regions: Two types of regions are at fictive temperature  $T_{\mathfrak{h}}$  pristine and photostrained, and two other types of regions have energy

distributions characteristic of the ambient temperature, but which also may be pristine or may be photostrained. Still, one can make several qualitative statements about the kinetics on the approach to a photochemical quasi-steady state. The structural relaxation of photoactivated regions is largely irreversible, while the dynamics in the ultrastable regions is largely arrested. The aging of the structure is then determined by the photoactivated spectrum, which is, however, time-dependent, because the structure of the glass is also changing with time under illumination. If the spectrum were considered to be static, the survival probability profile for the  $\alpha$ -relaxation spectra would be well-approximated by the stretched exponential  $e^{-(t/\tau_{\rm mp})^{\beta}}$ , where  $\tau_{\rm mp} = \tau_0 e^{F_{\rm mp}^{\pm}/k_B T}$  is the most probable relaxation time. The stretching exponent  $\beta$  would be small, since it is well-approximated by the expression  $^{33,59}$ 

$$\beta = \left[1 + \left(\frac{\delta F^{\ddagger}}{4k_{\rm B}T}\right)\right]^{-1/2} \approx \frac{4k_{\rm B}T}{\delta F^{\ddagger}} \tag{35}$$

with  $\delta F^{\ddagger}$  from eq 14. Note that photoactivation makes the dynamics resemble those of a fragile liquid, for which  $\delta F^{\ddagger}$  >  $4k_{\rm B}T$ . These semiquantitatve considerations already shed some light on the experimentally observed kinetics of photoinduced erasure of in-plane birefringence in the thin films of an azobenzene derivative.8 Erasure exhibits a slow regime wellapproximated by a power law  $t^{-T/T_m}$ , where the empirical parameter  $T_{\rm m}$  is larger for recordings that have been made using more intense exposure. We note that this slow, powerlike regime has been observed only over a modest range of erasing time, an order of magnitude or so. Thus, while the reported power-law kinetics seem to be slower than the stretched exponential, they are hard to distinguish from it. The exponent  $4k_{\rm B}T/\delta F^{\mp}$  from eq 35 and the exponent  $T/T_{\rm m}$  both show the same dependence on the temperature and amount of exposure to light during the recording. Indeed, the parameter  $\delta F^{\ddagger}$  is proportional to the most probable barrier. It effectively becomes larger as the sample becomes more stable. The reported aging kinetics appearing slower than the stretched exponential is consistent with the most probable relaxation time  $\tau_{\rm mp}^{-}$  itself growing linearly with time; see Appendix B.

Yet even the photoactivated dynamics becomes very sluggish, once the ambient temperature is sufficiently low. This results in several system-specific phenomena. An important example is provided by the low-temperature chalcogenide glasses  $^{20,74}$  that are subjected to macroscopic amounts of photons at supra-gap frequencies. Lubchenko and co-workers  $^{19,21,75}$  have suggested that the photoexcited electrons and holes that have failed to recombine become trapped in special orbitals, whose locations mirror the mosaic of the cooperatively reconfiguring regions that were frozen in at the glass transition. These special, electronically active defects reveal themselves through electron spin resonance (ESR) signals and midgap optical absorption,  $^{76,77}$  and they are removed only by prolonged annealing at sufficiently high temperatures. The magnitude of stored stress energy, per defect, was estimated  $^{19,21,75}$  to be  $\sim 10^1 k_{\rm B} T_{\rm g}$ , consistent with the present discussion.

We did not explicitly consider the possibility that crystallization or other local ordering processes can be induced by photoactivation. Several regimes of ordering in supercooled liquids and the glassy state have been discussed by Stevenson and Wolynes.<sup>68</sup> Generally, the lack of equilibrium in the glass provides extra destabilization with respect to those ordering processes. This makes possible nanocrystallization, already in the absence of photon activation. The photoactivation of crystallization is, in fact, the apparent mechanism underlying optical recording on rewritable optical drives. This way of recording information is not connected with the polarization of light but, instead, capitalizes on the distinct electro-optical properties of the glass and the crystal.

We finish this Section by a short discussion of how the yield strength of glasses is modified by photoactivation. The strength of glasses is one of their most remarkable features. It approaches the Frenkel limit<sup>78</sup> much more closely than do crystalline materials, which fail owing to dislocation motions. The above results for frozen glasses can be straightforwardly generalized to account for the effects of an additional external shear  $\Gamma$  by replacing  $\tilde{\varepsilon} \rightarrow \tilde{\varepsilon} + \frac{\Gamma^2 a^3}{2\mu} \times \frac{15(1-\sigma)}{(7-5\sigma)}$ , where  $\mu$  is the shear modulus.<sup>63</sup>

The  $T < T_g$  part of the "phase diagram" in Figure 6 can be interpreted as delineating the regime of mechanical stability of the glass. The  $T < T_g$  phase boundaries are nearly straight lines:  $\gamma' - \Delta c_p T_g \ln(T_g/T_K) - k_B T \ln\Omega - \tilde{\epsilon} \approx 0$ . Thus, we obtain a simple expression for the limiting strength of the glass, in the presence of photoactivation.

$$\frac{\Gamma_{\rm cr}^2 a^3}{2\mu} \frac{15(1-\sigma)}{(7-5\sigma)} = \gamma' - \Delta c_{\rm p} T_{\rm g} \ln(T_{\rm g}/T_{\rm K}) - k_{\rm B} T \ln \Omega - \tilde{\epsilon}$$
(36)

The initial weakening of glasses by light is shown in Figure 12, at  $T = T_K$ . At higher temperatures, the critical value of  $\Gamma$  is lowered

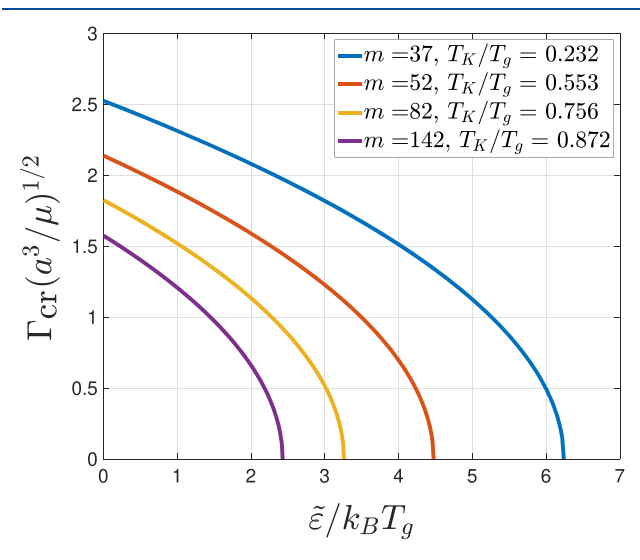


**Figure 12.** Dependence of the liming strength of the glass at  $T = T_K$  is plotted against the magnitude of the built-in photoactivated stress energy for select values of the fragility index. The corresponding values of  $T_K$  are indicated in the legend.

somewhat further. In any event, we observe that glasses can be substantially weakened at experimentally accessible values of photoinduced built-in stress, while fragile substances can be easily brought near mechanical breakdown! After phoinduced aging, however, the glass will become harder, as we have seen.

C. The Limit of Low Fluence. Percolation of Photoactivated Regions. We next consider the situation where only a small fraction of the molecules has become photoactivated so that isomerization events are well-separated in space and time. Because regions containing a photoexcited molecule are atypical, photoisomerization will only speed up the relaxation in the vicinity of the photoisomerized molecule. In this way, a photoactivated region can be thought of as a center of heterogeneous nucleation of structural relaxation. The local stress effectively picks out those activation paths for reconfiguration whose highest point can be stabilized by releasing that photoinduced stress. As a consequence, the local relaxation barriers for regions containing a chromophore are simply reduced by the amount  $\varepsilon_{\rm ph}$ .

$$F_{\rm ph}^{\ddagger} = F^{\ddagger} - \varepsilon_{\rm ph} \tag{37}$$

Also see Figure 13. Thus the whole barrier distribution for regions with a choromophore is shifted by a constant amount

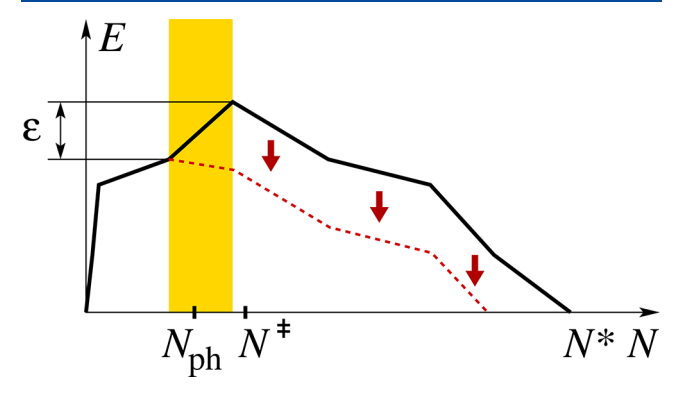


Figure 13. Schematic illustrating how the activation barrier is effectively lowered in the presence of built-in stress. The free energy profile is lowered through the photoactivated destabilization that occurs at the location  $N_{\rm ph}$  near the transition state.

nearly uniformly toward the low-barrier side. We will not address here the additional broadening due to the distribution of photoactivated stress energy  $\varepsilon_{\rm ph}$ .

For the very inhomogeneous situation arising in the low fluence limit, the consequences of facilitated dynamics reflected in eq 37 are different for the  $\alpha$ -and the  $\beta$ -processes, as we discuss next.

For the compact events that are the main contributors to  $\alpha$ relaxation, the most strained configuration is the transition state, in which  $N^{\ddagger}$  beads have already moved. Thus, the mole fraction  $x_{\alpha}$  of the sample that can be relaxed by the photoisomerizing moieties is given by

$$x_{\alpha} = n_{\rm ph} N^{\ddagger} a^3 \equiv n_{\rm ph} \xi^3 / 4 \tag{38}$$

where  $n_{\rm ph} = N_{\rm ph}/V$  is the concentration of photoexcited centers. This relation follows from the observation that the high point of the activation profile will be affected only if the isomerizing molecule occurs for a value  $N_{\rm ph}$  such that  $N_{\rm ph} < N^{\ddagger}$ ; see Figure 13. The remaining regions of the glass without isomerized molecules can only relax thermally. Consequently, the  $\alpha$ relaxation part of the barrier distribution is modified by photoactivation according to a mixing relation.

$$p_{\rm ph}^{(\alpha)}(F^{\ddagger}, x_{\alpha}) = (1 - x_{\alpha})p^{(\alpha)}(F^{\ddagger}) + x_{\alpha}p^{(\alpha)}(F^{\ddagger} + \varepsilon_{\rm ph})$$
(39)

In this equation, so as to avoid confusion, we emphasize that  $p^{(\alpha)}(F^{\ddagger})$  stands for the functional form of the barrier distribution for  $\alpha$ -relaxation that one has in the pristine sample. In other words, the quantity  $F^{\ddagger}$  in eq 39 is the argument of that functional form; it is not the most probable value of the barrier. The most probable value of the photoactivated portion of the distribution simply is shifted down by  $\varepsilon_{\rm ph}$  according to eq 37. Note that, in this "shifted" part of the distribution, the high-barrier cutoff is (approximately) determined by the most probable value  $F_{\alpha,\rm mp}^{\ddagger}$  of the *pristine* barrier distribution. For this reason, we suggest that one use the original Gaussian distribution derived by Xia and Wolynes<sup>33</sup> for this photoactivated contribution cut off at  $F_{\alpha,\rm mp}^{\ddagger}$  and properly normalized.

The barrier distribution in eq 39 depends (exponentially) on the temperature through the parameters in eq 13 but also algebraically through the T-dependence of the cooperativity length and, hence, the reweighting parameter  $x_{\alpha}$ . This dependence on the size of the cooperative region is actually quite substantial, as we illustrate in Figure 14. We note that the

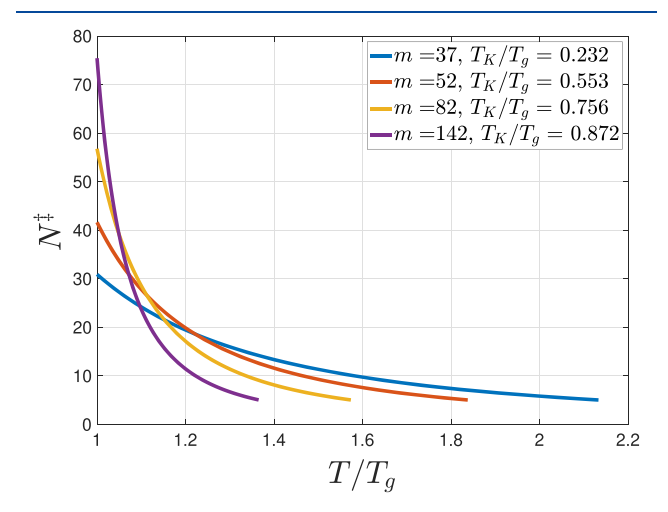


**Figure 14.** Temperature dependence of the typical transition-state size  $N^{\xi}$  for the  $\alpha$ -relaxations, from eq 9, for select values of the fragility index.

quantity on the rhs of eq 38 could be, in principle, greater than 1, because a region of size  $N^{\ddagger}$  may contain more than one isomerizable moiety, but in that case we should use the results obtained using the spatially averaging argument described in Subsection B. We emphasize that, by construction, eq 39 applies only for small concentrations of photoisomerized moieties. Equation 39 becomes nonsensical for  $x_{\alpha} > 1$ , of course. In any event, because of the elastic interactions between the photoinduced local stresses,  $^{79,80}$  photon-activated dynamics will percolate the sample already at values of  $x_{\alpha}$  less than 1, that is, well-before eq 39 becomes formally invalid. Interestingly, this percolation is progressively easier to achieve at lower temperatures, according to Figure 14.

At low levels of photoactivation, the distributions for the  $\beta$ -relaxation should *also* be a reweighted combination of the pristine and the "photostabilized" barrier distributions

$$p_{\rm ph}^{(\beta)}(F^{\ddagger}) = (1 - x_{\beta})p^{(\beta)}(F^{\ddagger}) + x_{\beta}p^{(\beta)}(F^{\ddagger} + \varepsilon_{\rm ph})$$
(40)

where the limit  $x_{\beta} \to 1$  of the mole fraction of photoactivated material nominally corresponds with stringy excitations becoming described by the spatially averaging results discussed earlier. As in the case of the  $\alpha$ -relaxation, the photoactivated contribution to the barrier distribution for  $\beta$ -relaxations is cut off, on the high barrier side, at the most probable value  $F_{\alpha,\rm mp}^{\ddagger}$  of the pristine barrier distribution.

In contrast with the  $\alpha$ -relaxation, below the crossover temperature the typical free energy profile for string growth is positively sloped throughout. Thus, the analogue of the critical size for capturing a photoisomerized unit in a region undergoing

 $\beta$ -relaxation is the full length of the string; a photoactivated unit will be able to release the strain within a region whose size is equal to the number of moves  $N_{\rm s}$  comprising the string. Thus, the reweighting factor should be

$$x_{\beta} = n_{\rm ph} \langle N_{\rm s} \rangle a^3 \tag{41}$$

where  $\langle N_s \rangle$  is the average string length. When  $x_\beta$  is very small, one may neglect the interactions between distinct strings, implying the detailed morphology of the string motion does not affect the estimate in eq 41. Such morphologies could be quite complicated, reflecting the complex physics in the crossover region.

We estimate the average length of the string in Appendix C at the same level of approximation described by Stevenson and Wolynes.<sup>32</sup> The average size turns out to be

$$\langle N_{\rm s} \rangle = \frac{1}{q \delta f^2} \{ F_{\alpha,\rm mp}^{\ddagger} \coth(F_{\alpha,\rm mp}^{\ddagger} q) - (F_{\alpha,\rm mp}^{\ddagger} - F_{\rm in})$$

$$\coth[(F_{\alpha,\rm mp}^{\ddagger} - F_{\rm in})q] \}$$
(42)

The temperature dependence of  $\langle N_{\rm s} \rangle$  in the  $[T_{\rm g}, T_{\rm cr}]$  range is exemplified for the same set of substances as in Figures 6 and 10. One notices that the average string length varies with temperature relatively little and remains modest in magnitude for fragile substances but can reach up to several tens near the crossover for strong fluids.

We note that, in contrast with the maximum string length, which would diverge at the crossover when we neglect string overlap, the average length remains finite even at the crossover,  $q \rightarrow 0$ , owing to the maximum barrier set by the  $\alpha$ -relaxation. Indeed, near the crossover the average string length becomes

$$\langle N_{\rm s} \rangle \xrightarrow[[q \to 0]]{} \frac{F_{\rm in}(2F_{\alpha,\rm mp}^{\ddagger} - F_{\rm in})}{3\delta f^2} \le \frac{(F_{\alpha,\rm mp}^{\ddagger})^2}{3\delta f^2} \tag{43}$$

This cutoff on the string stems ultimately from the facilitation effects, which essentially signal the overlap of many stringy reconfiguration events. The rest of the cumulants of the stringlength distribution are finite, too, consistent with the cutoff by the facilitation phenomena at the crossover; details on the distribution of the string length can be found in Appendix C. Furthermore, the average string length in fact must vanish if the initiation cost is zero, according to eq 42. The vanishing of the initiation cost implies the restoring force to bead movement is so small in the first place that already a vanishingly short string will lead to the destruction of the cage that serves to confine an individual bead.

Equations 40–(42) can be used to compute the  $\beta$ -part of the relaxation spectrum, which, together with the  $\alpha$ -part, should be used as input into the general formula 25. We expect that, even for modest levels of photoactivation, that is, for not too small  $x_{\alpha,\beta}$ , the resulting barrier distribution is still reasonably quantitatively useful so long as the corresponding reconfiguring regions have not yet percolated.

We note that the limit where the volumetric fraction  $x_{\beta}$  of the  $\beta$ -events goes to 1 does not actually correspond to a percolation of  $\beta$ -relaxation even in nominal terms.  $\beta$ -processes can be initiated only at a subset of locations. This fraction is reflected in the norm of the distribution  $\Psi$  being less than 1. Thus, a better estimate for the percolation threshold is given by the criterion

$$x_{\beta}\Psi \approx 1$$
 (44)

and not  $x_{\beta} \approx 1$ . Considering that  $\Psi$  decreases markedly below the crossover temperature, the multiplicative correction in eq 44 above is significant. In order for the crossover to take place, the string motions should be also marginally stable, of course<sup>31</sup>

$$\phi_{\rm ph} = 0 \tag{45}$$

where we assume that, because the percolation has taken place, it is appropriate to use the mean-field value of  $\phi_{\rm ph}$  from eq 29 relevant for the spatially averaged regime, not the pristine value from eq 18.

We infer from Figures 14 and 15 that the photoactivated part of the  $\beta$ -relaxation is largely suppressed, relative to the  $\alpha$ -part,

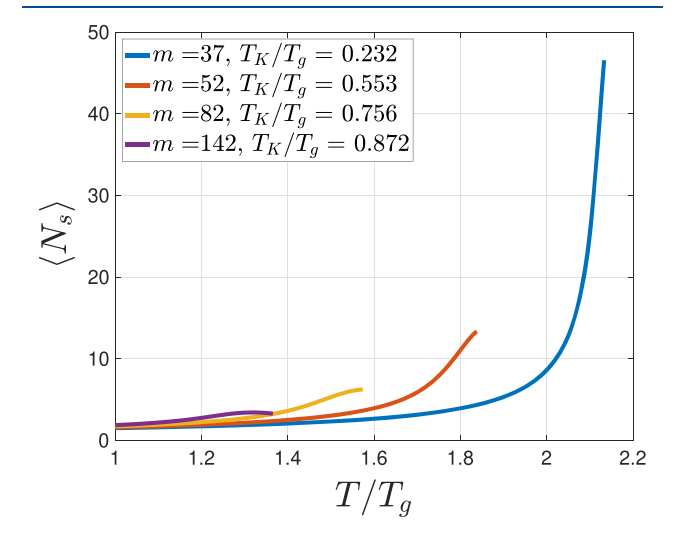
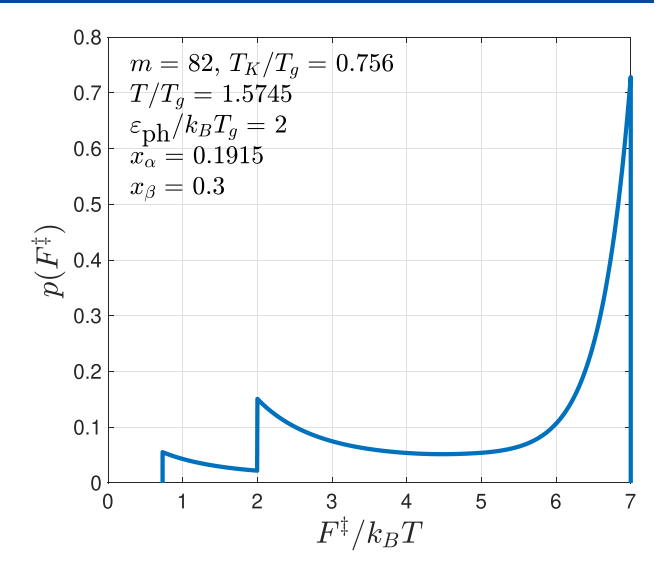


Figure 15. Temperature dependence of the typical string length  $N_s$  for the β-relaxations, for select values of the fragility index.

except for very strong substances and near the crossover. For the same reason, we anticipate that the percolation threshold for the  $\alpha$ -relaxation will usually occur under weaker illumination than what is needed for the  $\beta$ -relaxations.

We show an example of the photoactivated barrier distribution following a short intense pulse, in Figure 16, for a moderately fragile liquid near the crossover temperature. The value  $\varepsilon_{\rm ph} = 2k_{\rm B}T_{\rm g}$  is chosen so that the photoactivated stressmodified initiation free energy cost for string growth is still positive. (We remind the reader that  $\varepsilon_{\rm ph} \neq \tilde{\varepsilon}$ .) The first peak, proceeding from the left, corresponds to the photoactivated  $\beta$ relaxation contribution to the overall barrier distribution. The photoactivated  $\alpha$ -peak has merged with the  $\alpha$ -peak for the pristine peak. On the one hand, near  $T_{cr}$ , the barrier distribution for all substances looks qualitatively similar to the one shown in Figure 16, irrespective of the fragility. Near the laboratory  $T_{\sigma}$  on the other hand, the  $\beta$ -wing for strong substances is virtually absent, while for fragile liquids, only the pristine part of this wing is visible, as should be clear from Figures 14 and 15. We note that, in principle, the driving force  $\varepsilon_{\rm ph}$  can be made greater than  $F_{\rm in}$ , in which case the photoactivated contribution should be cut off at  $F^{\ddagger} = 0$ , while the corresponding weight added to the pristine contribution to  $p(F^{\ddagger})$ . Indeed, those regions where the photostabilized barrier  $F^{\ddagger}-\varepsilon_{\rm ph}$  is formally negative will have released their built-in stress very quickly, specifically, on the vibrational time scale  $\tau_0$ .

Photoinduced aging in frozen *glasses* in the low-fluence limit thus qualitatively resembles what is predicted using the spatially averaged formulas. Indeed, those regions that succeed in



**Figure 16.** Relaxation spectrum for a glassy melt above the glass transition temperature following a short, intense pulse of light of relatively low fluence. The value of the built-in stress energy  $\varepsilon_{\rm ph}$  per molecule, immediately following the pulse, is indicated on the graph.

structural relaxing will become stabilized. The new structure locally will be now be representative of the ambient temperature. Thus, in the course of a relatively prolonged illumination, one can expect a very rich relaxation spectrum that has up to eight distinct contributions, which may or may not be seen as separate peaks. These contributions can be thought of, respectively, as  $\alpha$ -and  $\beta$ -peaks corresponding to the four combinations that can be formed using two values of the fictive temperature and the two values of the built-in stress energy.

Finally we note the arguments here suggest that the dependence of the barrier distribution on  $N^{\ddagger}$  and  $\langle N_s \rangle$  can be used to quantify the temperature dependences of the cooperativity size for both relaxation types. Existing measurements and indeed direct observations via scanning micros $copy^{16,81-84}$  provide overwhelming evidence that the size  $\xi$  is on the scale of a few nanometers—consistent with predictions of the RFOT theory<sup>52</sup>—its detailed temperature dependence has so far been inferred relatively indirectly using bounds due to Berthier et al. 85 but again in agreement the RFOT theory. 6 In the absence of selectivity in the frequency of relaxation, these indirect experiments involve a weighted average of the quantities  $N^*$  and  $\langle N_s \rangle$ . Careful experimental studies of frequencydependent relaxation spectra, after photoactivation, should provide another way to separately determine the two dynamical correlation lengths.

## **IV. SUMMARY**

We have described how photoinduced isomerization activates the dynamics of viscous, glassy melts and frozen glasses proper. Low-viscosity solvents seem rather passive and exert little more than frictional damping on the isomerizing molecule; the molecule itself can be imagined as simply stirring the solvent. In contrast, glassy materials will first respond elastically when disturbed by a photoexcited molecule. This elastic response is a consequence of the transient breaking of the translational symmetry in the liquid as it is cooled below the dynamical crossover temperature. Both the emergence of the transient elasticity and the eventual structural relaxation of it—so as to restore the broken symmetry—we see can be quantitatively

described using the random first-order transition theory of

The built-in stress resulting from the photoexcitation serves to increase the driving force for the cooperative motions of the molecule and its environment on the combined free energy landscape. This stress energy can be determined calorimetrically by warming the sample sufficiently. The photoinduced increase in the driving force can be made so large that the structural reconfigurations can become completely barrierless, as they would be in a uniform liquid above the RFOT crossover. Applying shear further enhances this effect. In the absence of further irradiation, fluidized regions will quickly equilibrate at the ambient temperature. This means that, below the laboratory glass transition temperature, the glass will become more stable, following temporary fluidization. We estimated the amount of photoinduced built-in stress energy required to drive a glass to such a more stable state on a given time scale. A distinct possibility is that photoactivation can destabilize the amorphous state so much so as to induce crystallization. This is the mechanism of glass-to-crystal transformation in phase-change memory alloys.

Because an isomerizing molecule perturbs its environment only locally, within the cooperativity volume, photoactivation acts to enhance the already present heterogeneity even further. Thus, we have seen that, in addition to speeding up the structural dynamics overall, photoisomerization also broadens the relaxation spectrum. In terms of dynamics, this amounts to making even strong substances behave like their more fragile counterparts. Likewise, the photoactivation enhances the spatial aspect of the dynamical heterogeneity, which has particularly striking consequences below the laboratory glass transition. Following an intense pulse of light, the sample becomes a mosaic of regions of very widely distributed stability and relaxation rates. This spatial heterogeneity is of interest in its own right, as it provides a new possible test of glass transition theories, including the temperature dependence of the spatial extent of the cooperativity of structural relaxations. The heterogeneity in the stability of the glass can be also used as a practical way to record information. The present results are qualitatively consistent with the experimentally observed trends for optical writing and erasure in amorphous films that contain optically isomerizable molecules. In particular, the positive correlation between the stability of recording and the writing exposure directly follows from the present picture. The present results suggest that a more accurate treatment of the spatially heterogeneous dynamics of aging will yield the power-law kinetics writing/erasure observed in thin films, which is a subject of ongoing efforts by us.

# APPENDIX A: DETAILED PARAMETRIZATION OF THE LIQUID PROPERTIES

For the mismatch penalty coefficient  $\gamma$ , we will adopt the Lubchenko-Rabochiy approximation that emphasizes elastic

$$\gamma = (Ka^3k_BT)^{1/2} \tag{A1}$$

where *K* is the bulk modulus. Although not affecting the leading asymptotics  $T \to T_K$  of the temperature dependence of the  $\alpha$ relaxation barrier from eq 8, the detailed temperature dependence of the bulk modulus does vary sometimes substantially from substance to substance. This makes it difficult to write down a simple functional form for the temperature dependence

of the  $\alpha$ -relaxation barrier from eq 8 that would be accurate for a broad range of substances and in a wide temperature interval. Such an accurate description requires a detailed calculation. 46,72 At the same time, such a simple form is useful to illustrate the present results with the best clarity. As a compromise, here we adopt a particular parametrization in which the mismatch coefficient  $\gamma$  is temperature-independent:  $\partial \gamma / \partial T = 0$ . More complicated forms can be undoubtedly written down that yield better numerics; however, already this simple form reflects the fact that, for many substances, the bulk modulus decreases with temperature at a rate comparable to the growth of the linear function T. 51,72 (Note however that, for some strong substances, the modulus K actually increases mildly with temperature.  $^{72}$ )

The relations for the molecular inputs in eqs 32 and (A1), together with the RFOT predictions from eqs 8 and (11), give an  $\alpha$ -relaxation time  $\tau_{\alpha}$  described by the following simple functional form.

$$\ln(\tau_{\alpha}/\tau_{0}) = \frac{F_{\alpha,\text{mp}}^{\ddagger}}{k_{\text{B}}T} = \frac{\gamma^{2}T_{\text{K}}}{4\Delta c_{\text{p}}T_{\text{g}}} \frac{1}{T(T - T_{\text{K}})}$$
(A2)

Here  $\tau_0$  is the vibrational time scale of ca. 10 ps, which corresponds to viscosity values of order 1 cPs. It will be convenient to express quantities with the units of energy in terms of the kinetic glass transition temperature  $T_{\rm g}$ . We define this laboratory glass transition to be at the time scale corresponding to the Arrhenius exponent at  $T_g$  equal to some fixed number  $A_g$ .

$$\frac{F_{\alpha,\text{mp}}^{\ddagger}}{k_{\text{B}}T}\bigg|_{T=T_{\text{g}}} = A_{\text{g}}$$
(A3)

Again we will adopt the conventional value  $A_g = 37$  for concreteness. Assuming  $\tau_0 = 1 \times 10^{-12}$  s, this implies a kinetic glass transition defined on the laboratory time scale equal to  $10^{-12} \cdot e^{37}$  s  $\approx 0.3$  h.

At the thermal crossover to collisional transport, the Arrhenius exponent from eq A2 is predicted<sup>31,50,51</sup> to be a universal number so that  $\tau/\tau_0 = 10^3...10^4$ .

$$\frac{F_{\alpha,\text{mp}}^{\ddagger}}{k_{\text{B}}T}\bigg|_{T=T_{\text{cr}}} = A_{\text{cr}}$$
(A4)

For concreteness, we adopt  $A_{cr} = 7$ . Again, any of the temperatures  $T_{\rm g}$ ,  $T_{\rm K}$ , and  $T_{\rm cr}$  can be used as the energy scale,  $T_{\rm g}$  being the obvious choice because of its ready accessibility.

Given the constraints expressed in eq A3 and (A4), respectively, the temperature dependence of the most probable barrier is fully determined once one knows the apparent activation energy at the glass transition. This activation energy distinguishes strong from fragile systems through the so-called fragility index  $m = \partial \log_{10} \tau / \partial (T_g/T)$ . The fragility index then is

$$m = (\log_{10} e) A_{\rm g} \frac{2T_{\rm g} - T_{\rm K}}{T_{\rm g} - T_{\rm K}}$$
(A5)

According to the above equation, the smallest possible value of the fragility coefficient compatible with a positive  $T_{\rm K}$  is  $m_{\rm min}$  =  $2(\log_{10}(e))A_g \approx 32$ . Experimental values of m have been reported to be as low as 20 or so, which would apparently correspond with a negative  $T_{\rm K}$ . This observation poses no fundamental issues actually, as the temperature  $T_{\rm K}$ , at which the configurational entropy extrapolated to  $T < T_g$  vanishes, must be generally regarded as a fitting constant. Still, the functional form (32) is no longer physically acceptable for  $T_{\rm K}$  < 0, as it would imply a negative heat capacity. Thus, we will limit ourselves to the range  $m > m_{\rm min}$ , the smaller end of the range corresponding to strong substances, and the higher end to fragile substances.

Once we know  $T_{\rm g}$  and m, no additional parameters are needed to evaluate the relative width of the equilibrium barrier distribution in the absence of illumination, from eq 16.

$$\delta \tilde{F}_{\text{eq}} = \frac{\delta g}{\Delta g} \bigg|_{\text{eq}, n_{\text{ph}} = 0} = \left( \frac{T}{T_{\text{g}}} \frac{1}{4A_{\text{g}}(T_{\text{g}}/T_{\text{K}} - 1)} \right)^{1/2}$$
(A6)

Thus, the equilibrium barrier distribution for  $\alpha$ -relaxation and the crossover temperature are uniquely specified by the fragility alone. To fix the coefficient  $c_{\gamma}$  relating the mismatch coefficients  $\gamma$  and  $\gamma'$  from eqs 7 and (18), respectively, one however needs to separately specify the bulk modulus. Indeed, setting  $T = T_{\rm cr}$  and  $\phi = 0$  in eq 29 and using eq A1 yields straightforwardly

$$c_{\gamma} = \left(\frac{\tilde{K}^{1/2}}{4A_{\rm cr}} + \frac{\ln\left(\Omega\right)}{\tilde{K}^{1/2}}\right) \tag{A7}$$

where  $\tilde{K}_{\rm cr} \equiv Ka^3/k_{\rm B}T|_{T=T_{\rm cr}}$  is the dimensionless bulk modulus, at  $T=T_{\rm cr}$ . The quantity  $\tilde{K}$  is equal to the inverse square of the Lindemann ratio, up to a numerical factor. The Lindemann ratio is the vibrational displacement of a particle relative to the particle spacing and is expected to be nearly universal near the crossover. This circumstance then allows one to express  $\tilde{K}_{\rm cr}$  as a fixed number times a quantity that is determined by the Poisson ratio  $\sigma$ .

$$\tilde{K}_{cr} = B \frac{(1+\sigma)(5-6\sigma)}{3(1-2\sigma)(1-\sigma)} \tag{A8}$$

The numerical constant B in front of the fraction reflects the precise value of the Lindemann ratio at the temperature in question. In this paper we set B=10 in order to satisfactorily fit the values of the configurational entropy and the relaxation barrier over the entire temperature range while neglecting the temperature dependence of the mismatch coefficient  $\gamma$ . Thus, aside from the overall energy scale (and for a T-independent  $\gamma$ ), the dynamic properties of equilibrated glassy liquids can be specified by two dimensionless quantities, specifically, the fragility D and the Poisson ratio  $\sigma$ . The latter varies much less than the former, from substance to substance; here, we set the Poisson ratio at a generic value  $\sigma=0.25$ , for the sake of concreteness. This leads to  $\tilde{K}_{\rm cr}\approx 39$ . The quantity  $\ln\Omega$  is numerically close to 2, implying  $c_{\gamma}=0.54$ . This is not too different from the value  $c_{\gamma}=0.49$  adopted in ref 45 for hard spheres.

## APPENDIX B: TEMPORAL EVOLUTION OF THE TYPICAL RELAXATION TIME DURING AGING/REJUVENATION

Relaxations during aging/rejuvenation are overwhelmingly irreversible. One may thus write a diffusion equation for the time-dependent, photoactivated component of the barrier distribution  $p(F^\ddagger)$ , where the diffusivity is scaled by the Arrhenius factor  $e^{-F^\ddagger k_B T}$ . The high barrier edge  $F^\ddagger_{\max}$  of the distribution moves to the right with the rate scaling as the corresponding Arrhenius factor itself:  $\dot{F}^\ddagger_{\max} \propto e^{-F^\ddagger_{\max}/k_B T}$ . This immediately yields  $F^\ddagger_{\max} \propto \ln t$ , which, then, provides an upper

bound on the most probable relaxation time  $\tau_{\rm mp}$ . Thus, the typical relaxation time  $\tau_{\rm mp} = \tau_0 \, e^{F_{\rm mp}^\dagger/k_{\rm B}T} \propto t$ , up to a correction that depends on the detailed form of the (time-dependent) barrier distribution. The notion of the photoactivated part of the spectrum moving toward the high barrier side nominally corresponds with a microscopic setup, where the built-in stress is released in many small steps. In this case, the driving force becomes progressively smaller with each step, while the appropriate photoactivated spectrum gradually "drifts" toward the high-barrier side.

# **APPENDIX C:** BARRIER AND STRING-LENGTH DISTRIBUTION FOR β-RELAXATION

To determine the distributions of the barrier and the string length for the noncompact,  $\beta$ -subset of structural reconfigurations, we follow Stevenson and Wolynes<sup>32</sup> (SW). These authors picture string growth as a spatially contiguous set of bead moves. With eq 18, an individual move has an average driving force of  $-\partial F(N)/\partial N = -\phi$ , but this quantity fluctuates with root-mean-square deviation (rmsd) given by the quantity  $\delta f$  from eq 15. SW thus put forth a diffusion equation for the distribution  $\mathcal P$  of the overall energy cost x of making a string of length t

$$\frac{\partial \mathcal{P}}{\partial t} + \phi \frac{\partial \mathcal{P}}{\partial x} = \frac{\delta f^2}{2} \frac{\partial^2 \mathcal{P}}{\partial x^2} \tag{C1}$$

subject to the boundary conditions

$$\mathcal{P}(x=0) = \mathcal{P}(x=F^{\ddagger}) = 0 \tag{C2}$$

and the initial condition

$$\mathcal{P}(t=0) = \delta(x - F_{in}) \tag{C3}$$

since the string growth is subject to an initiation cost  $F_{\rm in}$ ;  $\delta(x)$  is the usual Dirac delta function. The quantity  $\delta f^2/2$  plays the role of the diffusivity. An *activation* barrier must be non-negative. By construction, the energy costs are constrained to not exceed a certain value  $F^{\ddagger}$ , giving rise to the boundary conditions (C2). Thus,  $\mathcal{P}(F^{\ddagger})$  is a cumulative distribution including the contributions of all trajectories that never grow larger than the given value  $F^{\ddagger}$ . The number of such excitation paths for all strings of length t that actually result in a relaxation is determined by the total "flux" through the origin, x=0.

$$\Psi(F^{\ddagger}, t) = \frac{\delta f^2}{2} \frac{\partial \mathcal{P}}{\partial x} \bigg|_{x=0}$$
 (C4)

When summed over all possible values of the string length *t*, the above expression gives the full cumulative distribution of the barrier

$$\Psi(F^{\ddagger}) = \int_0^{N_{\text{max}}} dt \Psi(F^{\ddagger}, t) \tag{CS}$$

while the corresponding probability density is simply

$$p^{(\beta)}(F^{\ddagger}) = \frac{\partial \Psi(F^{\ddagger})}{\partial F^{\ddagger}} \tag{C6}$$

Since the maximum activation barrier is bounded from above by  $F_{\rm mp}^{\ddagger}$ , owing to facilitation effects, the norm of this distribution, denoted in the main text by the letter  $\Psi$ , eq 23, is given by  $\Psi=\Psi(F_{\rm mp}^{\ddagger})$ . It is understood that  $F_{\rm in} < F_{\rm in}^{\ddagger} < F_{\rm mp}^{\ddagger}$ .

For the Laplace transform  $\tilde{\mathcal{P}}(s) = \int_0^\infty dt e^{-st} \mathcal{P}(t)$ , eq C1 yields

$$s\tilde{\mathcal{P}} - \delta(x - F_{\rm in}) + \phi \frac{\partial \tilde{\mathcal{P}}}{\partial x} = \frac{\delta f^2}{2} \frac{\partial^2 \tilde{\mathcal{P}}}{\partial x^2}$$
 (C7)

The "drift" term  $\partial \tilde{P}/\partial x$  can be dealt with by introducing a new function  $\tilde{P}_{\phi} \equiv e^{-x\phi/\delta f^2} \tilde{P}$ . This yields

$$\frac{\delta f^2}{2} \frac{\partial^2 \tilde{\mathcal{P}}_{\phi}}{\partial x^2} - \left( s + \frac{\phi^2}{2\delta f^2} \right) \tilde{\mathcal{P}}_{\phi} = -\delta (x - F_{\rm in}) e^{-F_{\rm in}\phi/\delta f^2}$$
(C8)

Note the functions  $\tilde{\mathcal{P}}$  and  $\tilde{\mathcal{P}}_{\phi}$  are also subject to the boundary conditions (C2), which, then, allows one to expand the function  $\tilde{\mathcal{P}}_{\phi}$  in terms of the sine functions  $\sin(\pi nx/F^{\ddagger})$ ,  $n=1, 2, ..., \infty$ . After following through with a straightforward calculation, one may present  $\tilde{\mathcal{P}}$  as an infinite series.

$$\tilde{\mathcal{P}}(s) = \sum_{n=1}^{\infty} \frac{\frac{2}{L} \sin\left(\frac{\pi n F_{\text{in}}}{F^{\ddagger}}\right) \sin\left(\frac{\pi n x}{F^{\ddagger}}\right)}{\frac{df^{2}}{2} \left(\frac{\pi n}{F^{\ddagger}}\right)^{2} + \left(s + \frac{\phi^{2}}{2\delta f^{2}}\right)}$$
(C9)

With the help of eq C4 and formula (1.445.1) of Gradshtein and Ryzhik, <sup>86</sup> one then obtains a very manageable expression for the Laplace image  $\tilde{\Psi}(F^{\ddagger}, s) = \int_0^{\infty} dt e^{-st} \Psi(F^{\ddagger}, t)$ .

$$\tilde{\Psi}(F^{\ddagger}, s) = \frac{\sinh\left[\frac{F^{\ddagger} - F_{\text{in}}}{\delta f} \left(2s + \frac{\phi^2}{\delta f^2}\right)^{1/2}\right]}{\sinh\left[\frac{F^{\ddagger}}{\delta f} \left(2s + \frac{\phi^2}{\delta f^2}\right)^{1/2}\right]}$$
(C10)

The expression for the original  $\Psi(F^{\ddagger},t)$  is not nearly as simple, however. To invert the Laplace transform in the expression above we first note that, while the numerator and denominator each have a branch cut along the  $(-\infty, -\phi^2/2\delta f^2]$  ray on the real axis, the fraction itself does not. Still, employing an integration contour that would be appropriate for the latter branch cut, see, for instance, ref 87, one can show that the Laplace original can be presented as a sum over the residues of the rhs of eq C10. The residues are exclusively located on the aforementioned ray. Either of the two Riemann sheets of the square root can be used as long as one is being consistent with using the same sheet for both the numerator and denominator. This yields the following series expansion.

$$\Psi(F^{\ddagger}, t) = \left(\frac{df}{F^{\ddagger}}\right)^{2} e^{-(t/2)\left(\frac{\phi}{df}\right)^{2}} \sum_{m=1}^{\infty} (-1)^{1+m} e^{-(t/2)\left(m\frac{df}{F^{\ddagger}}\right)^{2}} m$$

$$\sin\left[m\frac{\pi(F^{\ddagger} - F_{\text{in}})}{F^{\ddagger}}\right]$$
(C11)

We note this expression can be expressed as a derivative of the Jacobi theta function  $\theta_4$ . One may check that the above distribution is normalizable—the norm itself equal to  $\tilde{\mathcal{P}}(F^\ddagger,0)$ , of course—while noting that all of its moments  $\langle t^n \rangle$  are finite. In fact, the higher the moment, the better the respective sum converges. In practice, it is easier to compute the moments and the corresponding cumulants by evaluating, respectively, the derivatives of the Laplace transform from eq C10 and its logarithm at s=0.

The above statement on the finiteness of the moments and cumulants of the distribution  $\Psi(F^{\ddagger}, t)$  is valid even at the crossover, where  $\phi = 0$ , and the maximum possible string length thus diverges. We note that, at  $\phi = 0$ , the cumulants happen to

have a particularly simple form. For the cumulant of order n,  $K_{n}$ , one has

$$K_n(\phi = 0) = (-1)^n \frac{\partial^n}{\partial s^n} \ln \tilde{\Psi}(F^{\ddagger}, s)|_{s=0, \phi=0}$$
 (C12)

$$=c_n \frac{(F^{\ddagger})^{2n} - (F^{\ddagger} - F_{\text{in}})^{2n}}{\delta f^{2n}}$$
(C13)

$$\leq c_n \left(\frac{F^{\ddagger}}{\delta f}\right)^{2n} \tag{C14}$$

where the numerical coefficients  $c_n$  can be found by Taylor-expanding  $\ln \tilde{\Psi}(F^{\ddagger},s)_{\phi=0}$  around s=0. For instance,  $c_1=1/3$ ,  $c_2=16/945$ ,  $c_3=16/945$ ,  $c_4=16/1575$ ,  $c_5=256/31185$ . Thus, we see that the string-length distribution is quite compact, which is already clear from the series in eq C11, whose leading asymptotics in the string length t are similar to the  $1/k_BT \rightarrow \infty$  asymptotics of the partition function for a particle in the box. We observe that, already in the absence of the force  $\phi$ , which confines string growth, there is an intrinsic upper bound for the string length determined by the length scale  $(F^{\ddagger}/\delta f)^2$ . The latter length essentially determines the "time" it takes to "diffuse" from one edge of the box to the other. The quantity  $(F^{\ddagger}/\delta f)^2$  can be as large as a hundred or so for very strong substances but, usually, is substantially smaller, as we discuss in the main text.

Away from the crossover, where  $\phi > 0$ , the string length will be determined by the smallest of the following three length scales: (1) the cutoff length  $N_{\rm max} = F_{\rm mp}^{\ddagger}/\phi$  (see eqs 22 and (C5)), (2) the drift length scale  $(\delta f/\phi)^2$  (see the exponential in front of the sum in eq C11), and (3) the "intrinsic" length scale from eq C13. Sufficiently far away from the crossover, the latter intrinsic length is well-approximated by  $2c_1F^{\ddagger}F_{\rm in}/\delta f^2$ , which is less than the absolute upper bound  $(F^{\ddagger}/\delta f)^2$ .

In view of the complicated functional form of the string-length distribution in eq C11, it is practical to replace the hard cutoff in eq C5 by a softer, exponential cutoff, which, note, preserves the normalization.

$$\Psi(F^{\ddagger}) \approx \int_0^\infty d t e^{-t/N_{\text{max}}} \Psi(F^{\ddagger}, t)$$
 (C15)

This approximation was employed by Stevenson and Wolynes.<sup>32</sup> With their approximation, the cumulative distribution of the barrier heights is simply equal to

$$\Psi(F^{\ddagger}) \approx \tilde{\Psi}(F^{\ddagger}, 1/N_{\text{s,max}}) \tag{C16}$$

where  $\tilde{\Psi}$  is the Laplace transform from eq C10. Now, differentiating the above quantity with respect to  $F^{\ddagger}$  yields the probability density for the  $\beta$ -relaxation barriers given as eq 20 of main text. Setting the argument of the cumulative distribution (C16) to its maximum possible value,  $F^{\ddagger} = F^{\ddagger}_{mp}$ , produces the norm of the barrier distribution  $\Psi$ , eq 23 of the main text. The expressions for the distributions obtained here, specifically from eqs 20 and (23), differ somewhat from those obtained by Stevenson and Wolynes, the latter also containing an extra factor  $e^{-F_{in}\psi/\delta f^2}$ .

Furthermore, we note that the integrand in eq C15 now becomes the effective distribution for the string length t, if one sets  $F^{\ddagger} = F^{\ddagger}_{\rm mp}$  in that equation, while the nominal maximum length is infinite. Accordingly, the Laplace transform  $\tilde{\Psi}(F^{\ddagger}_{\rm mp},s)$ , with  $\tilde{\Psi}(F^{\ddagger},s)$  from eq C10, can be regarded as the moment-generating function of this string-length distribution. This is

analogous to the way the partition function is the generating function for the energy distribution. Likewise the quantity  $\ln \tilde{\Psi}(F_{\rm mp}^{\ddagger}, s)$  is the cumulant-generating function of the stringlength distribution. Because the latter distribution is not normalized to unity, the expectation value for the string length is most conveniently found by computing the first cumulant. Thus, we compute the latter expectation value  $\langle t \rangle \equiv \langle N_s \rangle$  by differentiating  $\ln \tilde{\Psi}(F_{\rm mp}^{\ddagger}, s)$  with respect to (-s) and then setting  $s = 1/N_{s, \rm max} = \phi/F_{\rm mp}^{\ddagger}$ . The result is given as eq 42 of the main text.

#### AUTHOR INFORMATION

#### **Corresponding Authors**

Vassiliy Lubchenko — Departments of Chemistry and Physics, and Texas Center for Superconductivity, University of Houston, Houston 77204-5003, Texas, United States; ○ orcid.org/0000-0001-6398-261X; Email: vas@uh.edu

Peter G. Wolynes — Departments of Chemistry, Physics and Astronomy, Biosciences, Materials Science and Nanoengineering, and the Center for Theoretical Biological Physics, Rice University, Houston 77005, Texas, United States; orcid.org/0000-0001-7975-9287; Email: pwolynes@rice.edu

Complete contact information is available at: https://pubs.acs.org/10.1021/acs.jpcb.0c06515

#### **Notes**

The authors declare no competing financial interest.

#### ACKNOWLEDGMENTS

V.L.'s work is supported by the NSF Grant Nos. CHE-1465125 and CHE-1956389, the Welch Foundation Grant No. E-1765, and a grant from the Texas Center for Superconductivity at the University of Houston. P.G.W.'s work is supported by the Center for Theoretical Biological Physics sponsored by the National Science Foundation (NSF Grant No. PHY-1427654). Additional support to P.G.W. was provided by the D. R. Bullard-Welch Chair at Rice University (Grant No. C-0016). We thank Peter Rossky for many enlightening and enjoyable conversations over many decades.

## **■** REFERENCES

- (1) Bodenstein, M. Die chemischen wirkungen des lichts. Naturwissenschaften 1929, 17, 788-795.
- (2) Kistiakowsky, G. B. The action of light on chlorine. *J. Am. Chem. Soc.* **1927**, 49, 2194–2200.
- (3) Norrish, R. G. W.; Porter, G. Chemical reactions produced by very high light intensities. *Nature* **1949**, *164*, 658–658.
- (4) Velsko, S. P.; Fleming, G. R. Photochemical isomerization in solution. photophysics of diphenyl butadiene. *J. Chem. Phys.* **1982**, *76*, 3553–3562.
- (5) Lubchenko, V.; Wolynes, P. G. Theory of Structural Glasses and Supercooled Liquids. *Annu. Rev. Phys. Chem.* **2007**, *58*, 235–266.
- (6) Lubchenko, V. Theory of the structural glass transition: A pedagogical review. *Adv. Phys.* **2015**, *64*, 283–443.
- (7) Xu, W.-C.; Sun, S.; Wu, S. Photoinduced reversible solid-to-liquid transitions for photoswitchable materials. *Angew. Chem., Int. Ed.* **2019**, *58*, 9712–9740.
- (8) Fang, G. J.; Maclennan, J. E.; Yi, Y.; Glaser, M. A.; Farrow, M.; Korblova, E.; Walba, D. M.; Furtak, T. E.; Clark, N. A. Athermal photofluidization of glasses. *Nat. Commun.* **2013**, *4*, 1521.
- (9) Zhang, Z.-Y.; He, Y.; Wang, Z.; Xu, J.; Xie, M.; Tao, P.; Ji, D.; Moth-Poulsen, K.; Li, T. Photochemical phase transitions enable coharvesting of photon energy and ambient heat for energetic molecular solar thermal batteries that upgrade thermal energy. *J. Am. Chem. Soc.* **2020**, *142*, 12256–12264.

- (10) Claudé, B.; Gonon, L.; Verney, V.; Gardette, J. Consequences of photoageing on the durability of plastic glasses for automotive applications. *Polym. Test.* **2001**, *20*, 771–778.
- (11) Kozdras, A.; Golovchak, R.; Shpotyuk, O.; Szymura, S.; Saiter, A.; Saiter, J.-M. Light-assisted physical aging in chalcogenide glasses: Dependence on the wavelength of incident photons. *J. Mater. Res.* **2011**, 26, 2420–2427.
- (12) Lucas, P.; Doraiswamy, A.; King, E. A. Photoinduced structural relaxation in chalcogenide glasses. *J. Non-Cryst. Solids* **2003**, 332, 35–42
- (13) Gueguen, Y.; Sangleboeuf, J. C.; Keryvin, V.; Lépine, E.; Yang, Z.; Rouxel, T.; Point, C.; Bureau, B.; Zhang, X.-H.; Lucas, P. Photoinduced fluidity in chalcogenide glasses at low and high intensities: A model accounting for photon efficiency. *Phys. Rev. B: Condens. Matter Mater. Phys.* **2010**, 82, 134114.
- (14) Yannopoulos, S. N.; Trunov, M. L. Photoplastic effects in chalcogenide glasses: A review. *Phys. Status Solidi B* **2009**, 246, 1773—1785.
- (15) Lyubin, V.; Klebanov, M.; Mitkova, M.; Petkova, T. Polarization-dependent, laser-induced anisotropic photocrystallization of some amorphous chalcogenide films. *Appl. Phys. Lett.* **1997**, *71*, 2118–2120.
- (16) Nguyen, D.; Nienhaus, L.; Haasch, R. T.; Lyding, J.; Gruebele, M. Sub-nanometer glass surface dynamics induced by illumination. *J. Chem. Phys.* **2015**, *142*, 234505.
- (17) Mott, N. F.; Davis, E. A. Electronic Processes in Non-crystalline Materials; Clarendon Press: Oxford, UK, 1979.
- (18) Mott, N. F. Conduction in Non-crystalline Materials; Clarendon Press: Oxford, UK, 1993.
- (19) Zhugayevych, A.; Lubchenko, V. An intrinsic formation mechanism for midgap electronic states in semiconductor glasses. *J. Chem. Phys.* **2010**, *132*, 044508.
- (20) Zhugayevych, A.; Lubchenko, V. Electronic structure and the glass transition in pnictide and chalcogenide semiconductor alloys. II: The intrinsic electronic midgap states. *J. Chem. Phys.* **2010**, *133*, 234504.
- (21) Lukyanov, A.; Golden, J. C.; Lubchenko, V. Structural origin of the midgap electronic states and the urbach tail in pnictogen-chalcogenide glasses. *J. Phys. Chem. B* **2018**, *122*, 8082–8097.
- (22) Fleming, G.; Wolynes, P. G. Chemical dynamics in solution. *Phys. Today* **1990**, 43, 36–43.
- (23) Bowman, R. M.; Eisenthal, K. B. The role of translational friction in isomerization reactions. *Chem. Phys. Lett.* **1989**, *155*, 99–101.
- (24) Rothenberger, G.; Negus, D. K.; Hochstrasser, R. M. Solvent influence on photoisomerization dynamics. *J. Chem. Phys.* **1983**, *79*, 5360–5367.
- (25) McCaskill, J. S.; Gilbert, R. G. Fokker-Planck interpretation of picosecond intramolecular dynamics in solutions. *Chem. Phys.* **1979**, *44*, 389–402.
- (26) Waldeck, D. H. Photoisomerization dynamics of stilbenes. *Chem. Rev.* **1991**, 91, 415–436.
- (27) Voth, G. A.; Hochstrasser, R. M. Transition State Dynamics and Relaxation Processes in Solutions: A Frontier of Physical Chemistry. *J. Phys. Chem.* **1996**, *100*, 13034–13049.
- (28) Ishida, T.; Rossky, P. J. Consequences of strong coupling between solvation and electronic structure in the excited state of a betaine dye. *J. Phys. Chem. B* **2008**, *112*, 11353–11360.
- (29) Neukirch, A. J.; Shamberger, L. C.; Abad, E.; Haycock, B. J.; Wang, H.; Ortega, J.; Prezhdo, O. V.; Lewis, J. P. Nonadiabatic ensemble simulations of cis-stilbene and cis-azobenzene photo-isomerization. *J. Chem. Theory Comput.* **2014**, *10*, 14–23.
- (30) Lubchenko, V.; Wolynes, P. G. Theory of aging in structural glasses. J. Chem. Phys. 2004, 121, 2852–2865.
- (31) Stevenson, J. D.; Schmalian, J.; Wolynes, P. G. The shapes of cooperatively rearranging regions in glass-forming liquids. *Nat. Phys.* **2006**, *2*, 268–274.
- (32) Stevenson, J. D.; Wolynes, P. G. A universal origin for secondary relaxations in supercooled liquids and structural glasses. *Nat. Phys.* **2010**, *6*, 62–68.

- (33) Xia, X.; Wolynes, P. G. Microscopic theory of heterogeneity and nonexponential relaxations in supercooled liquids. *Phys. Rev. Lett.* **2001**, *86*, 5526–5529.
- (34) Teboul, V.; Saiddine, M.; Nunzi, J.-M. Isomerization-induced dynamic heterogeneity in a glass former below and above  $T_{\rm g}$ . *Phys. Rev. Lett.* **2009**, *103*, 265701.
- (35) Teboul, V.; Accary, J.-B.; Chrysos, M. Isomerization of azobenzene and the enhancement of dynamic heterogeneities in molecular glass formers. *Phys. Rev. E* **2013**, *87*, 032309.
- (36) Teboul, V.; Accary, J. B. Induced cooperative motions in a medium driven at the nanoscale: Searching for an optimum excitation period. *Phys. Rev. E* **2014**, *89*, 012303.
- (37) Swallen, S. F.; Kearns, K. L.; Mapes, M. K.; Kim, Y. S.; McMahon, R. J.; Ediger, M. D.; Wu, T.; Yu, L.; Satija, S. Organic glasses with exceptional thermodynamic and kinetic stability. *Science* **2007**, *315*, 353–356.
- (38) Beasley, M. S.; Bishop, C.; Kasting, B. J.; Ediger, M. D. Vapor-Deposited Ethylbenzene Glasses Approach "Ideal Glass" Density. *J. Phys. Chem. Lett.* **2019**, *10*, 4069–4075.
- (39) Bagchi, K.; Ediger, M. D. Controlling structure and properties of vapor-deposited glasses of organic semiconductors: Recent advances and challenges. *The Journal of Physical Chemistry Letters* **2020**, *11*, 6935–6945, DOI: 10.1021/acs.jpclett.0c01682.
- (40) Pergushov, V.; Bormot'ko, O.; Gurman, V. Photoisomerization of azoethane in hydrocarbon glasses at 77 K. Effect of the "matrix memory". *Chem. Phys. Lett.* **19**77, *S1*, 269–272.
- (41) Kasha, M. Characterization of electronic transitions in complex molecules. *Discuss. Faraday Soc.* **1950**, *9*, 14–19.
- (42) Lubchenko, V. A Universal Criterion of Melting. *J. Phys. Chem. B* **2006**, *110*, 18779—18786.
- (43) Landau, L. D.; Lifshitz, E. M. Theory of Elasticity; Pergamon Press: New York, 1986.
- (44) Lubchenko, V.; Wolynes, P. G. Intrinsic quantum excitations of low temperature glasses. *Phys. Rev. Lett.* **2001**, *87*, 195901.
- (45) Lubchenko, V.; Wolynes, P. G. Aging, jamming, and the limits of stability of amorphous solids. *J. Phys. Chem. B* **2018**, *122*, 3280–3295.
- (46) Lubchenko, V.; Rabochiy, P. On the mechanism of activated transport in glassy liquids. J. Phys. Chem. B 2014, 118, 13744–13759.
- (47) Tool, A. Q. Relation between inelastic deformability and thermal expansion of glass in its annealing range. *J. Am. Ceram. Soc.* **1946**, 29, 240–253.
- (48) Narayanaswamy, O. S. A model of structural relaxation in glass. *J. Am. Ceram. Soc.* **1971**, *54*, 491–498.
- (49) Moynihan, C. T.; Easteal, A. J.; Bolt, M. A.; Tucker, J. Dependence of the fictive temperature of glass on cooling rate. *J. Am. Ceram. Soc.* **1976**, *59*, 12–16.
- (50) Rabochiy, P.; Lubchenko, V. Universality of the onset of activated transport in Lennard-Jones liquids with tunable coordination: Implications for the effects of pressure and directional bonding on the crossover to activated transport, configurational entropy and fragility of glassforming liquids. *J. Chem. Phys.* **2012**, *136*, 084504.
- (51) Rabochiy, P.; Lubchenko, V. Liquid state elasticity and the onset of activated transport in glass formers. *J. Phys. Chem. B* **2012**, *116*, 5729–5737.
- (52) Xia, X.; Wolynes, P. G. Fragilities of liquids predicted from the random first order transition theory of glasses. *Proc. Natl. Acad. Sci. U. S. A.* **2000**, *97*, 2990–2994.
- (53) Berthier, L.; Biroli, G. Theoretical perspective on the glass transition and amorphous materials. *Rev. Mod. Phys.* **2011**, 83, 587–645.
- (54) Lubchenko, V.; Wolynes, P. G. The origin of the boson peak and thermal conductivity plateau in low temperature glasses. *Proc. Natl. Acad. Sci. U. S. A.* **2003**, *100*, 1515–1518.
- (55) Lubchenko, V.; Wolynes, P. G. The microscopic quantum theory of low temperature amorphous solids. *Adv. Chem. Phys.* **2008**, *136*, 95–206.
- (56) Kirkpatrick, T. R.; Thirumalai, D.; Wolynes, P. G. Scaling concepts for the dynamics of viscous liquids near an ideal glassy state. *Phys. Rev. A: At., Mol., Opt. Phys.* **1989**, *40*, 1045–1054.

- (57) Bhattacharyya, S. M.; Bagchi, B.; Wolynes, P. G. Facilitation, complexity growth, mode coupling, and activated dynamics in supercooled liquids. *Proc. Natl. Acad. Sci. U. S. A.* **2008**, *105*, 16077—16082.
- (58) Bhattacharyya, S. M.; Bagchi, B.; Wolynes, P. G. Bridging the gap between the mode coupling and the random first order transition theories of structural relaxation in liquids. *Phys. Rev. E* **2005**, *72*, 031509.
- (59) Lubchenko, V. Charge and momentum transfer in supercooled melts: Why should their relaxation times differ? *J. Chem. Phys.* **2007**, 126, 174503.
- (60) Stickel, F.; Fischer, E. W.; Richert, R. Dynamics of glass-forming liquids. II. Detailed comparison of dielectric relaxation, dc-conductivity, and viscosity data. *J. Chem. Phys.* **1996**, *104*, 2043–2055.
- (61) Stevenson, J. D.; Wolynes, P. G. A universal origin for secondary relaxations in supercooled liquids and structural glasses. *Nat. Phys.* **2009**, *6*, 62–68.
- (62) Lubchenko, V.; Wolynes, P. G. In Structural Glasses and Supercooled Liquids: Theory, Experiment, and Applications; Wolynes, P. G., Lubchenko, V., Eds.; John Wiley & Sons, 2012; pp 341–379.
- (63) Wisitsorasak, A.; Wolynes, P. G. On the strength of glasses. *Proc. Natl. Acad. Sci. U. S. A.* **2012**, *109*, 16068–16072.
- (64) Wisitsorasak, A.; Wolynes, P. G. Fluctuating mobility generation and transport in glasses. *Phys. Rev. E* **2013**, *88*, 022308.
- (65) Tatsumisago, M.; Halfpap, B. L.; Green, J. L.; Lindsay, S. M.; Angell, C. A. Fragility of Ge-As-Se glass-forming liquids in relation to rigidity percolation, and the Kauzmann paradox. *Phys. Rev. Lett.* **1990**, 64, 1549–1552.
- (66) Richert, R.; Angell, C. A. Dynamics of glass-forming liquids. V. On the link between molecular dynamics and configurational entropy. *J. Chem. Phys.* **1998**, *108*, 9016.
- (67) Lubchenko, V.; Wolynes, P. G. Barrier softening near the onset of nonactivated transport in supercooled liquids: Implications for establishing detailed connection between thermodynamic and kinetic anomalies in supercooled liquids. *J. Chem. Phys.* **2003**, *119*, 9088–9105.
- (68) Stevenson, J. D.; Wolynes, P. G. The ultimate fate of supercooled liquids. *J. Phys. Chem. A* **2011**, *115*, 3713–3719.
- (69) Xia, X.; Wolynes, P. G. Diffusion and the mesoscopic hydrodynamics of supercooled liquids. *J. Phys. Chem. B* **2001**, *105*, 6570–6573.
- (70) Wolynes, P. G. Spatiotemporal structures in aging and rejuvenating glasses. *Proc. Natl. Acad. Sci. U. S. A.* **2009**, *106*, 1353–1358.
- (71) Wisitsorasak, A.; Wolynes, P. G. Dynamical heterogeneity of the glassy state. *J. Phys. Chem. B* **2014**, *118*, 7835–7847.
- (72) Rabochiy, P.; Wolynes, P. G.; Lubchenko, V. Microscopically based calculations of the free energy barrier and dynamic length scale in supercooled liquids: The comparative role of configurational entropy and elasticity. *J. Phys. Chem. B* **2013**, *117*, 15204–15219.
- (73) Qiu, Y.; Antony, L. W.; de Pablo, J. J.; Ediger, M. D. Photostability can be significantly modulated by molecular packing in glasses. *J. Am. Chem. Soc.* **2016**, *138*, 11282–11289.
- (74) Lukyanov, A.; Lubchenko, V. Amorphous chalcogenides as random octahedrally bonded solids: I. implications for the first sharp diffraction peak, photodarkening, and boson peak. *J. Chem. Phys.* **2017**, 147, 114505.
- (75) Zhugayevych, A.; Lubchenko, V. Electronic structure and the glass transition in pnictide and chalcogenide semiconductor alloys. I: The formation of the  $pp\sigma$ -network. J. Chem. Phys. **2010**, 133, 234503.
- (76) Biegelsen, D. K.; Street, R. A. Photoinduced Defects in Chalcogenide Glasses. *Phys. Rev. Lett.* **1980**, 44, 803–806.
- (77) Hautala, J.; Ohlsen, W. D.; Taylor, P. C. Optically induced electron-spin resonance in  $As_xS_{1-x}$ . *Phys. Rev. B: Condens. Matter Mater. Phys.* **1988**, 38, 11048–11060.
- (78) Frenkel, J. Zur theorie der elastizitätsgrenze und der festigkeit kristallinischer körper. Eur. Phys. J. A 1926, 37, 572–609.
- (79) Bevzenko, D.; Lubchenko, V. Stress distribution and the fragility of supercooled melts. *J. Phys. Chem. B* **2009**, *113*, 16337–16345.

- (80) Bevzenko, D.; Lubchenko, V. Self-consistent elastic continuum theory of degenerate, equilibrium aperiodic solids. *J. Chem. Phys.* **2014**, *141*, 174502.
- (81) Tracht, U.; Wilhelm, M.; Heuer, A.; Feng, H.; Schmidt-Rohr, K.; Spiess, H. W. Length scale of dynamic heterogeneities at the glass transition determined by multidimensional nuclear magnetic resonance. *Phys. Rev. Lett.* **1998**, *81*, 2727–2730.
- (82) Vidal Russell, E.; Israeloff, N. E. Direct observation of molecular cooperativity near the glass transition. *Nature* **2000**, *408*, 695–698.
- (83) Cicerone, M. T.; Ediger, M. D. Enhanced translation of probe molecules in supercooled *o*-terphenyl: Signature of spatially heterogeneous dynamics? *J. Chem. Phys.* **1996**, *104*, 7210–7218.
- (84) Ashtekar, S.; Scott, G.; Lyding, J.; Gruebele, M. Direct Visualization of Two-State Dynamics on Metallic Glass Surfaces Well Below *T<sub>o</sub>. J. Phys. Chem. Lett.* **2010**, *1*, 1941–1945.
- (85) Berthier, L.; Biroli, G.; Bouchaud, J.-P.; Cipelletti, L.; el Masri, D.; L'Hôte, D.; Ladieu, F.; Perino, M. Direct experimental evidence of a growing length scale accompanying the glass transition. *Science* **2005**, 310, 1797–1800.
- (86) Gradstein, I. S.; Ryzhik, I. M. Table of Integrals, Series and Products; Academic Press, 1994.
- (87) Lubchenko, V.; Silbey, R. J. Interrupted Escape and the Emergence of Exponential Relaxation. J. Chem. Phys. 2004, 121, 5958.